High stress drop and slow rupture during the 2020 M_W6.4 Petrinja earthquake, Croatia

Iva Lončar[1]*, Mathieu Causse[2], Martin Vallée[3], Snježana Markušić[1]

[1] University of Zagreb, Faculty of Science, Department of Geophysics, Zagreb, Croatia

[2] Université Grenoble-Alpes, Université Savoie Mont Blanc, CNRS, IRD, UGE, ISTerre, Grenoble, France

[3] Institut de Physique du Globe de Paris, CNRS, Sorbonne Paris Cité, Paris, France

* iva.loncar@gfz.hr

Abstract

Here we analyze the rupture process of the December 29th, 2020 M_W6.4 Petrinja earthquake (Croatia), the largest event recorded in this area characterized by a moderate strain-rate intraplate setting. We use foreshocks and aftershocks, recorded at more than 80 broadband stations located 70km to 420km from the earthquake, as empirical Green's functions (EGFs) to separate source effects from propagation and local site effects. First, we deconvolve the mainshock P-wave time windows from the EGFs in the frequency domain to obtain the corner frequency (f_c). Spectral analysis based on a Brune's source model reveals a large stress drop of 24 MPa. Next, by deconvolving the Love waves in the time domain, we calculate the Apparent Source Time Functions (ASTFs). We find that the average duration of the source is ~5 s, with no significant directivity effects, indicating a bilateral rupture. To extract physical rupture parameters such as rupture velocity, slip distribution and rise time, we deploy two techniques: (1) Bayesian inversion and (2) backprojection onto isochrones of ASTFs. Both techniques show a low rupture velocity (40-50% of the shear wave velocity) and a rupture length of less than 10 km, i.e. much less than would typically be expected for a magnitude 6.4 earthquake. This apparent anticorrelation between stress drop and rupture velocity may be attributed to the complex and segmented fault system characteristic of immature intraplate settings.

Keywords: Petrinja earthquake 2020, Seismological data, Empirical Green's Functions, Rupture analysis, Source model, Seismic hazard, Bayesian kinematic inversion, Backprojection

1. Introduction

The Croatian territory, situated at the convergence of three significant geological units—the Alps to the northwest, the Pannonian basin to the east, and the Dinarides to the south (Ustaszewski et al., 2008)—exhibits a moderate level of seismic activity, occasionally experiencing strong earthquakes (magnitude > 6). Most earthquakes in this area stem from strain accumulation driven by the Adria microplate's rotation towards the Eurasian tectonic plate (Anderson & Jackson, 1987, Calais et al.,

2002, Battaglia et al., 2004, Ustaszewski et al., 2010). The Croatian Earthquake Catalogue (CEC), updated and first described in Herak et al. (1996), documents over 150 earthquakes with a magnitude greater than 5, that occurred in Croatia or the neighboring countries in the last 100 years.

In terms of seismic activity, year 2020 was critical for Croatia and Croatian people, with the occurrence of two destructive earthquakes: the M_L5.5 Zagreb event on the 22nd of March and the M_W6.4 Petrinja event on the 29th of December. These events occurred approximately 70 km apart, both resulting in human casualties and extensive damage. This study focuses on the 2020 Petrinja earthquake, one of the most powerful recorded events in the region, surpassing the expected magnitude for this area (Markušić et al., 2021), and also one of the strongest in Europe since the 2016 M_W 6.5 central Italy earthquake. This area holds particular significance as it was the location of the 1909 Kupa Valley earthquake, that Andrija Mohorovičić used for his discovery of the Mohorovičić Discontinuity (MOHO) between the Earth's crust and mantle (Herak & Herak, 2010).

In the early morning, at 6:28 local time on December 28th, 2020, a moderate M_L5.0 earthquake, the first foreshock of the sequence, struck the broader Petrinja area. In the next 29 hours, this event was followed by 38 additional foreshocks, including a significant M_L4.7 earthquake occurring less than two hours after the initial one. The subsequent day, on December 29th at 12:19, the powerful M_W6.4 mainshock struck the region. The epicentral intensity reached VIII-IX °EMS indicating its destructive power. The earthquake was felt in a radius of at least 400 km, with reports of people sensing the shaking in Croatia, Bosnia and Herzegovina, Slovenia, Serbia, Austria, Hungary, Italy, and even Czechia (Markušić et al., 2021). Seven people lost their lives, dozens were injured, and thousands remained homeless because of the extensive damage of towns and villages close to the epicenter (such as Sisak, Petrinja, Glina, Majske Poljane, etc.; Miranda et al., 2021). Furthermore, the intense ground shaking led to secondary destructive effects such as liquefaction and collapse of underground sinkholes, particularly in the vicinity of Mečenčani village. There, over a hundred sinkholes collapsed, including one with a diameter exceeding 20 meters (Markušić et al., 2021; Baize et al., 2022).

The M_W6.4 Petrinja mainshock occurred in a moderate strain-rate intraplate setting on the complex Petrinja-Pokupsko fault system (Xiong et al., 2021; Baize et al. 2022). Source and ground motion features of intraplate earthquakes are still poorly understood, due to relatively low seismicity rates and sparse station distribution (e.g. Viegas et al., 2010; Onwuemeka et al., 2018). This further underscores the significance of a comprehensive and meticulous analysis of the seismic source and its impact on ground shaking for enhancing future seismic hazard assessments.

In this study, our primary aim is to determine the rupture process of the M_W6.4 Petrinja mainshock. We first use seismological data located at distances between 70 and 420 km to obtain Apparent Source

Time Functions (ASTFs) in the framework of a point source model, both in the frequency and time domain. The ASTFs are next inverted within a Bayesian framework, to obtain stress drop and kinematic source parameters, including the effective dimensions of rupture, the distribution of final slip, rupture velocity, and rise time, and the associated uncertainties. We also deploy an alternative technique, referred to as backprojection of ASTFs, which is free of inversion. We next discuss the inferred rupture properties in light of the tectonic setting. Given the absence of near-fault strong motion recordings in the observed area, the obtained kinematic rupture model provides us source parameters necessary for subsequent near-fault strong motion simulations. This is an important issue for improving seismic hazard assessment in the region but also more generally in moderate strain-rate intraplate environments.

2. Seismological data

To constrain the mainshock source parameters, we use seismological data (see section Data availability) recorded at 83 stations all over Italy, Slovenia, Austria, Slovakia, Hungary, Croatia, Bosnia and Hercegovina, and Montenegro, which results in a good azimuthal coverage (Figure 1). As will be detailed subsequently, seismograms are deconvolved from wave propagation effects both in the frequency domain (stations indicated with blue triangles) and in the time domain (stations indicated with yellow triangles). We use data from stations at epicentral distances ranging from approximately 70 km to 420 km, all sampled at 50 Hz and band-pass filtered between 0.01 Hz and 20 Hz. We exclusively utilize data with a signal-to-noise ratio exceeding 2, a point that will be elaborated upon later.

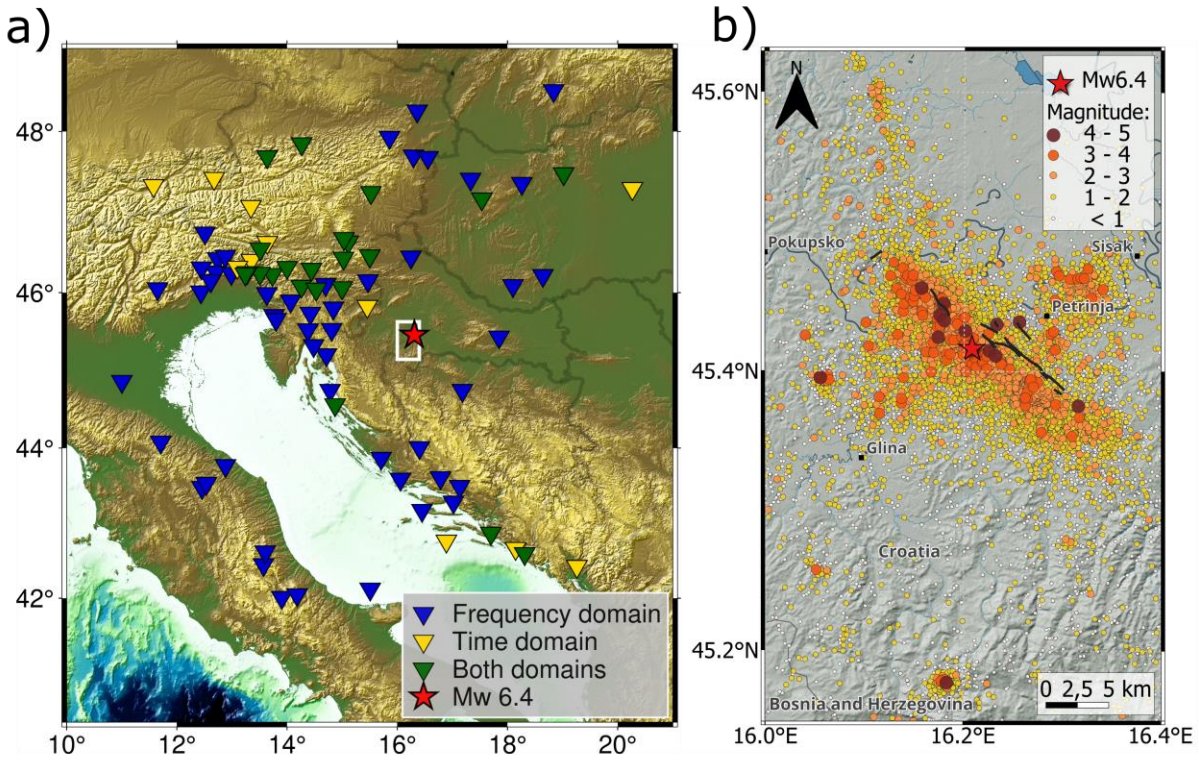

Figure 1. Station distribution and Petrinja earthquake sequence. a) The color of the triangles indicates the type of analysis for which each station has been used (frequency-domain or time-domain deconvolution). The red star shows the epicenter of the mainshock. The area indicated with a white rectangle is zoomed in on figure 1b; b) Epicenters of Petrinja earthquake sequence until the end of 2021. Black lines represent co-seismic rupture trace (Baize et al., 2022).

2.1 Empirical Green's Function analysis

To analyze the behavior of an earthquake source, it is necessary to isolate the source effect from the seismic waveform recorded at the seismic station. In the framework of a point source model, an earthquake seismogram, *s(t)*, results from the convolution of earthquake source effects *e(t)*, propagation and local site effects *G(t),* and the known instrument response *I(t)*:

$$s(t) = e(t) * G(t) * I(t). \quad (1)$$

When we aim to isolate source effects alone, the concept of Empirical Green's Function (EGF) analysis comes into play. This method is founded on the assumption that suitable foreshocks or aftershocks, which can be used as EGFs, efficiently model propagation and local site effects. According to Lay and Wallace (1995), an earthquake preceding or following the mainshock can serve as an EGF if it meets the following criteria: 1) it exhibits an almost identical focal mechanism as the mainshock; 2) the hypocentral depth closely matches that of the mainshock; 3) the earthquake's magnitude is high enough to provide a satisfactory Signal-to-Noise Ratio (*SNR*) but simultaneously low enough to

minimize the influence of its own source effects compared to the mainshock. To satisfy the last condition, it is preferable to have an earthquake with a magnitude at least two units smaller than the one of the mainshock.

In this study, we consider six earthquakes as potential EGF candidates (Table 1) with magnitudes exceeding 4. We have first checked that the selected EGFs have coefficients of correlation with the mainshock exceeding 0.7. Among these six observed earthquakes, EGF2 emerges as the optimal candidate, and it is subsequently utilized in our research.

Table 1. Earthquakes considered as potential EGF candidates.

Event label	Date	Time (UTC)	Position (°N, °E)	Magnitude
EGF1	09.01.2021.	21:29	45.413, 16.217	4.2
EGF2	06.01.2021.	17:01	45.412, 16.206	4.7
EGF3	30.12.2020.	05:26	45.442, 16.179	4.6
EGF4	30.12.2020.	05:15	45.439, 16.167	4.8
EGF5	28.12.2020.	06:49	45.424, 16.236	4.6
EGF6	28.12.2020.	05:28	45.369, 16.351	5.1

Our analysis of the source process is divided into three steps: 1.) Frequency-domain EGF deconvolution, in which we compute corner frequency as a function of azimuth, and compute stress drop assuming a circular crack model; 2.) Time-domain EGF deconvolution, to infer Apparent Source Time Functions (ASTFs), representing the source time function "seen" from a seismic station (e.g. Mueller, 1985; Chounet et al., 2018); 3.) Lastly, we present a kinematic source model obtained using kinematic inversion and backprojection of the ASTFs.

2.2 Frequency-domain EGF deconvolution

Frequency-domain EGF deconvolution provides insights into stress drop and potential directivity effects. Here we mostly follow the procedure described in Abercrombie et al. (2016).

First, all waveforms are resampled at 50 Hz. Second, we manually select body waves from the recordings. While the analysis can be performed on both *P* and *S* waves, we use here *P* waves because they are easier to pick. We use a time-window length of *nsec* = 30 s, as proposed by Abercrombie et al. (2016) for such a magnitude. For the closest stations, for which T_S-T_P < 30 s, *nsec* is chosen equal to T_S-T_P. Using a Butterworth filter, we then bandpass filter our data within the range of f_{min} = 1/*nsec* and f_{max} = 5 Hz.

We select only frequencies of the *P*-wave spectra with a signal-to-noise ratio (*SNR*) greater than 2. Additionally, we cross-correlate EGF events waveforms with those of the mainshock, retaining only those with cross-correlation above 0.7 (Abercrombie et al., 2016). We perform this using EGF2, EGF5, and EGF6, but, as mentioned, focus on results obtained using EGF2 waveforms. Since it is not expected that the mainshock and the EGF candidate correlate well at frequencies above the corner frequency of the stronger event (Abercrombie, 2015), the P windows are bandpass filtered between 1/*nsec* and 0.2 Hz before computing cross-correlation. We tested various cross–correlation values (0.4 – 0.8) to compromise good azimuthal coverage with more stations and data quality.

After isolating the *P*-wave windows of the mainshock and well-correlated EGFs, we compute displacement and Fourier spectra. We approximate the source process with a "ω^{-2} model" (Aki, 1967; Brune, 1970) assuming that an earthquake can be represented by a circular crack in an elastic medium (Brune, 1970). Subsequently, to calculate the corner frequencies, we conduct Brune's spectrum fitting on averaged spectral ratio for each station. The theoretical spectral ratio has the following form:

$$\frac{\dot{M}_1(f)}{\dot{M}_2(f)} = \frac{M_{01}}{M_{02}} \left(\frac{1+(f/f_{c2})^{\gamma n}}{1+(f/f_{c1})^{\gamma n}} \right)^{1/\gamma}. \quad (2)$$

In equation 2, f represents frequency, f_{c1} and f_{c2} are the corner frequencies for the mainshock and EGF earthquakes, with the seismic moments of M_{01} and M_{02} respectively. n is a factor representing high-frequency fall-off assumed as n = 2, and a constant γ controls the shape of the corner, which we set to a value γ = 1 based on Brune (1970). Before fitting, the spectra obtained at any station from all EGF recordings and components are stacked. By spectral stacking and computation of the mean spectrum for each station, we minimize the uncertainties and ensure more stable estimates (Kane, 2011) resulting in less biased results than when individually fitting each spectral ratio (Abercrombie, 2016). We then perform Brune's spectrum fitting using grid search following Viegas et al. (2010) to obtain corner frequencies of the mainshock and the EGF, f_{c1} and f_{c2}, respectively. For the grid search we use frequency step of 0.01 Hz in the range 0.03 Hz - 5 Hz. To quantify uncertainties, we perform Bayesian estimates of the model parameters as proposed in Causse et al. (2021). Figure 2a illustrates the whole process for station VENJ of the Croatian network and displays Joint Probability Density Functions of the parameters f_{c1} and f_{c2}. Note that we only use f_{c1}, which is much better resolved than the EGF corner frequency f_{c2}.

With knowledge of seismic moment and corner frequency, we can compute stress drop using Equation 3 (e.g. Madariaga,1976, and Eshelby, 1957):

$$\Delta\sigma = \frac{7M_0}{16} \frac{f_c^3}{k^3 \beta^3} \quad (3)$$

159 Focusing on *P*-waves, the *k* value equals 0.32, and we use a shear wave velocity (*β*) of 3400 m/s, based
160 on the Balkan model (B.C.I.S., 1972).

161 We calculate corner frequencies for each station, and compute the mean values for azimuthal classes
162 of 45° (Figure 2c). Subsequently, we compare the obtained azimuthal variations of the corner
163 frequencies with the values obtained for a line source model assuming unilateral or bilateral rupture
164 scenarios (see Supplementary Material S1) to investigate the overall rupture behavior. The
165 comparison indicates weak azimuthal variations of the corner frequency, which is consistent with a
166 bilateral rupture.

167 Additionally, we calculate an average corner frequency (f_c) value of 0.24 Hz, obtained by fitting the
168 spectral ratio stacking over all stations. From Equation (3), this gives a stress drop of 24 MPa. This
169 average stress drop exceeds the expected value for shallow intraplate earthquakes, which is about 6
170 MPa (Allmann & Shearer, 2009). Note that we run the procedure for various values of *nsec* and cross-
171 correlation thresholds. For instance, using *nsec* = 20 s give a stress drop of 27 MPa. Furthermore, using
172 a cross-correlation threshold of 0.8 results in a stress drop of 20 MPa. Despite this uncertainty, our
173 analysis indicates a large stress drop value. This conclusion is also supported by findings of Xiong et al.
174 (2022), reporting a stress drop of 27 MPa.

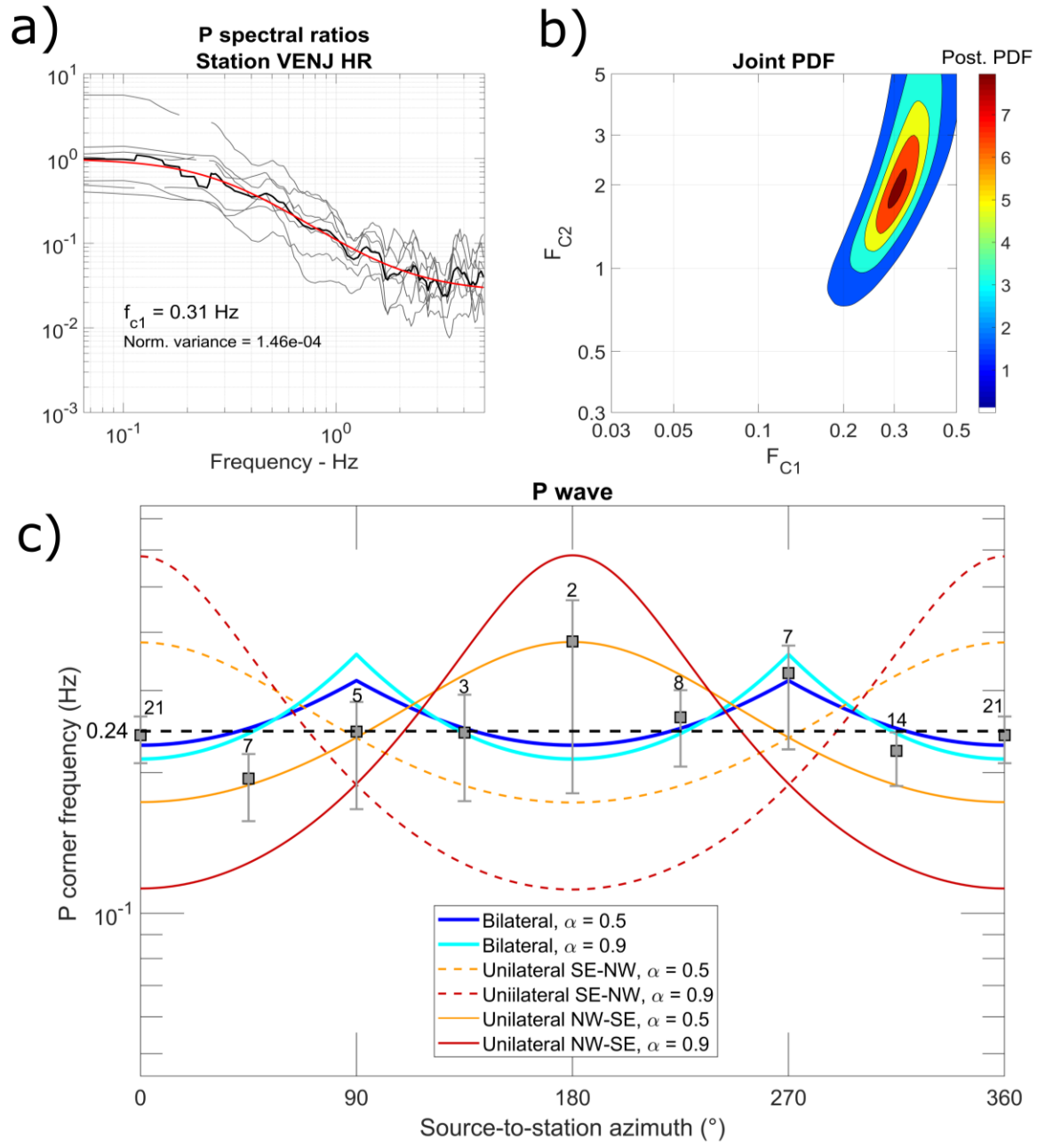

Figure 2. Corner frequency determination. a) Ratios between mainshock and EGFs *P*-wave spectra used for f_c computation at Venje (Croatia) station. The black curve represents the average and the red curve the best-fitting model; b) Joint Probability Density Function (PDF) of the mainshock and EGF corner frequency at Venje (Croatia) station (F_{C1} and F_{C2} respectively); c) Computed f_c values from seismic data with respect to source-station azimuth, compared to the theoretical values for a line source model with unilateral and bilateral ruptures (see Supplementary Material 1). α represents represents the ratio between the rupture velocity and the *P*-wave velocity. Stations at 0° are situated along the mainshock fault strike to the Northwest. Numbers on the error bars indicate the number of used stations in the given source-to-station azimuth range. The theoretical curves are obtained using Eq. S1.1 and S1.2 of Supplementary material S1. The value of the takeoff angle is assumed to be 50°.

2.3. Time-domain EGF deconvolution

The next step involves computing Source Time Functions (STFs) using the EGF method. These functions display the release of seismic moment over time as fractures propagate, revealing insights into the dislocation history (e.g. Convertito et al., 2021). As STFs are distorted by the source-station geometry and the type of waves used, we refer to them as Apparent Source Time Functions (ASTFs). The duration of the ASTFs mirrors the source duration observed at each station. Similar to the frequency domain deconvolution, adequate azimuthal coverage is essential to ensure reliable constraints for parameter calculations in subsequent stages (e.g. Chounet et al., 2018). Though ASTFs were primarily derived using body waves from mainshocks and smaller events (e.g., Mueller, 1985), we use surface waves due to their dominance in the waveforms and superior signal-to-noise ratios. Velasco et al. (1994) highlight that the two-dimensional radiation patterns of surface waves offer more consistent deconvolutions and encompass a wider range of directivity parameters compared to body waves. Here we focus on Love waves, which are dominant for the nearly vertical strike-slip rupture of the Petrinja mainshock. As Love waves propagate horizontally, they accentuate azimuthal variations of ASTFs contributing to better resolution of kinematic rupture parameters. In addition, the horizontal propagation eliminates potential uncertainties associated to take-off angles of body waves.

We thus use the transversal components of both main and EGF waveforms. Firstly, we bandpass filter waveforms within the range 0.02-0.1 Hz. Secondly, we manually pick mainshock and EGF Love wave windows. We then shift the mainshock by 1.5 s, a technique deployed for handling the difficulty to properly identify the Love wave arrival times and to avoid obtaining non-causal ASTFs (i.e. starting with non-zero values).

The goal of the deconvolution process is to find an ASTF that, when convolved with the EGF Love-wave window, closely matches the mainshock Love-wave window. We use the projected Landweber algorithm, imposing constraints of positivity, causality, and bounded duration of the ASTFs (Bertero et al., 1997; Vallée, 2004). We measure the level of fit as (1 – misfit) × 100%, where misfit is the ratio between the Euclidean norm of the residuals and of the data. We conduct a two-stage process in which we increase frequency to obtain more detailed ASTFs.

First, we conduct the deconvolution process on waveforms that are low-pass filtered up to 0.1 Hz (Figure 3a), selecting only stations where the fit between observed and modeled waveforms exceeds 90%. Subsequently, for the selected stations, we repeat this process but using a low-pass filter at 0.5 Hz (Figure 3b). We then retain ASTFs with a fit level above 60%. After obtaining the ASTFs for each station, we manually align them and suppress non-physical features. This involves removing values

below 10% of the maximum ASTF value, as well as eliminating isolated bumps and ASTFs showing abnormally elongated or irregular shapes suggestive of non-physical slow rupture initiation or termination in the source. To determine the source duration, we follow the method of Courboulex et al. (2016), measuring the span of the ASTF from its initial amplitude exceeding 0.1 times the peak value (*Fm*), displaying an increasing trend, to the final amplitude above 0.1 times *Fm* with a decreasing trend.

The lower level of fit obtained for the frequency range 0.02-0.5 Hz (Figure 3) may be explained by Love wave dispersion, or the difficulty to reproduce higher frequency source details with inherently imperfect EGF, implying for instance a different excitation of higher Love mode for the mainshock. As such, the proposed two-stage deconvolution allows us to obtain robust ASTFs, while getting more detailed information about the source.

To further test the robustness of the inferred ASTFs, we perform the analysis using EGF2, EGF5, and EGF6 to obtain ASTFs and corresponding source durations (Supplementary Material S2). To characterize the uncertainty due to the use of various EGFs on the ASTFs duration, we compute the standard deviation of the natural logarithm residuals of duration, where logarithm residual for station *I* and each EGF is defined as $\overline{\ln(T_i)}$. When considering all stations and all EGFs, we obtain a value of 0.08, indicating uncertainty of less than 10%. While the results show little dependence on the selected EGF, further analyses are conducted using EGF2, which provides the largest number of adequate ASTFs.

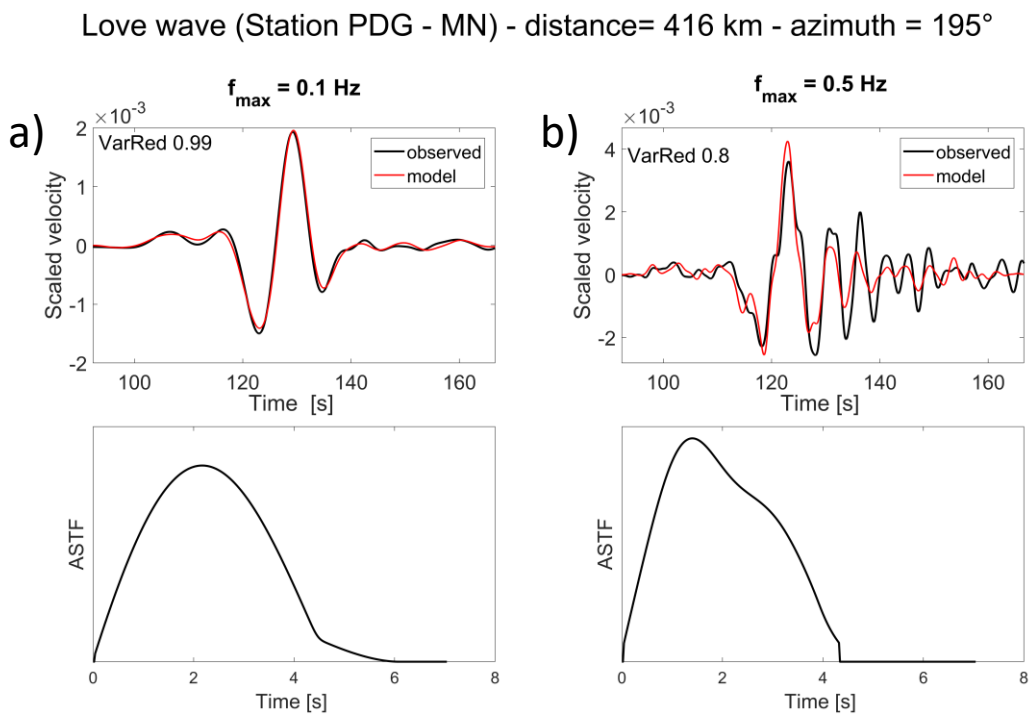

239

240 **Figure 3.** Results of the EGF deconvolution process at PDG station. Comparison between simulated
241 and observed data are shown in the top panel and obtained ASTFs are shown in the bottom panel.
242 Mainshock and EGF data have been lowpass filtered below f_{max} = 0.1 Hz (a) or f_{max} = 0.5 Hz (b).

243 The above described procedure results in 33 ASTFs. Despite some gaps in azimuthal coverage,
244 especially between 135° to 180° of source-receiver azimuths due to limited data or station availability,
245 we did not observe significant variability in source duration (Figure 4). Our results indicate ASTFs with
246 rather abrupt termination and source durations between 4 and 6 seconds, with an average duration
247 of 5 seconds. This later value is lower than the average expected source duration of approximate 8 s
248 reported by Courboulex et al. (2016) for a M_w6.4 event (excluding subduction events). This is
249 consistent with the study of Houston (2001), where shallow intraplate events show shorter durations
250 and more abrupt source function terminations compared to events occurring in more active tectonic
251 settings.

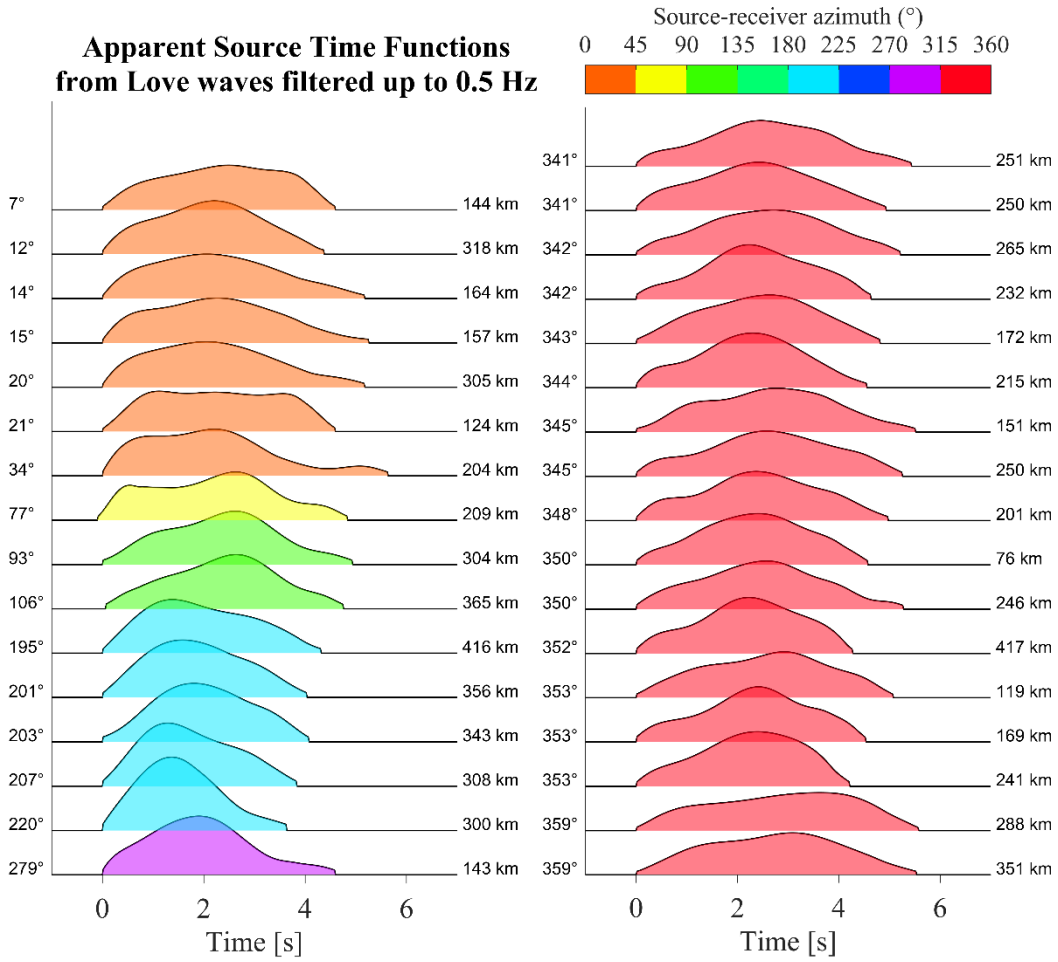

Figure 4. ASTFs obtained from EGF deconvolution using Love waves low-pass filtered at f_{max}=0.5 Hz.

Note that EGF deconvolution provide ASTFs for the mainshock under the assumption that the EGF represents the impulse response of the medium. However, the real EGF duration is finite. Based on frequency-domain deconvolution (section 2.2), EGF2 has corner frequency ranging between 1 and 1.5 Hz. Despite the large uncertainty on f_{c2}, this is consistent with an expected corner frequency of ~1 Hz for a M_W4.7 event (e.g. Allmann & Shearer, 2009). Source duration is related to corner frequency by $T = \alpha / fc$ with α between 1 s and 1.7 s, depending on the source model (e.g. Courboulex et al., 2016), which leads to an EGF duration between 0.3 s and 1 s. Here we assume a duration of 0.7 s. We then correct the ASTFs by convolving them with a 0.7 s boxcar function. This set of corrected ASTFs is used in the following to obtain rupture parameters.

3. Finite Source Modelling

3.1 Backprojection of ASTFs on isochrones

We first use a method called “isochrone backprojection” to obtain the kinematic source parameters from the ASTFs (Király-Proag et al., 2019). The method does not rely on inversion and provides fast estimates of the source parameters. It relies on the notion of isochrone, which represents the set of points on the fault that radiate seismic energy arriving at a given time *t* at the station (Figure S3). Since the seismic energy arrival time is the sum of the wave arrival time (Love wave in our case) and the rupture time, the computation of the isochrones requires *a priori* assumption on the rupture velocity and hypocenter position. Here, we assume a constant rupture velocity and a rupture initiation at 7.8 km depth (Baize et al., 2021). The basic principle of the method is then to distribute the ASTFs (representing the apparent moment rate) observed at each station uniformly on its isochrones, at different time steps, thus providing the space-time evolution of seismic moment on the fault. It is important to note that the seismic moment release at a particular locus on the fault is spread out over the isochrones. As such the method provides a defocused image of the actual seismic moment release areas, the accuracy of which is defined by the intersection between the isochrone contributions of all stations (Festa & Zollo, 2006).

In order to improve focusing, we use an iterative procedure in which the residuals between ASTFs at iterations *i* and *i+1* are back-projected to obtain a new slip model (e.g. Beroza & Spudich, 1988). At the first iteration, the slip model obtained from back-projecting the original ASTFs is used to compute synthetic ASTFs. At the second iteration, the slip model obtained from the backprojection of the residuals, defined as the difference between original and synthetic ASTFs, is added to the slip model from the first iteration. The new slip model is used in turn to generate new ASTFs. The process is interrupted when the misfit - defined as the L2-norm between ASTFs at iterations *i* and *i+1* - stops decreasing, within a limit of 8 iterations. Since the procedure requires the reconstruction of synthetic ASTFs at each iteration, it also implies assuming *a priori* value of the rise time. The procedure is therefore run for various values of rupture velocity and rise time, and the rupture model with the minimum misfit is finally selected. The whole process is illustrated by synthetic tests, in which synthetic ASTFs are generated assuming three 4x4 km slip patches at various depths (Figure 5). The results indicate that while the size and position of the slip patch located above the hypocenter is fairly well resolved, the slip patches located at 5-10 km each side of the hypocenter are smeared along the fault dip. Such a poor vertical resolution is inherent to the use of Love waves. It arises because isochrones beyond ~5 km from the hypocenter are predominantly vertical for horizontally propagating Love waves, whatever the source-station azimuth, resulting in a vertical smearing of the slip patches. The along-strike position of the slip patches remains however correct.

Figure 6 shows the obtained slip map for the M_w6.4 Petrinja earthquake, indicating a rupture length of roughly 10 km. The minimum misfit is obtained for a rupture velocity of 1.7 km/s (≈0.5V_S) and a rise time of 0.5 s. The slip map corresponds to an approximately 10x8 km^2 slip patch located above the hypocenter. Despite the tradeoff between the rupture velocity and the rise-time (Figure 6), the results point to a slow propagating rupture with $V_R < 0.6V_S$.

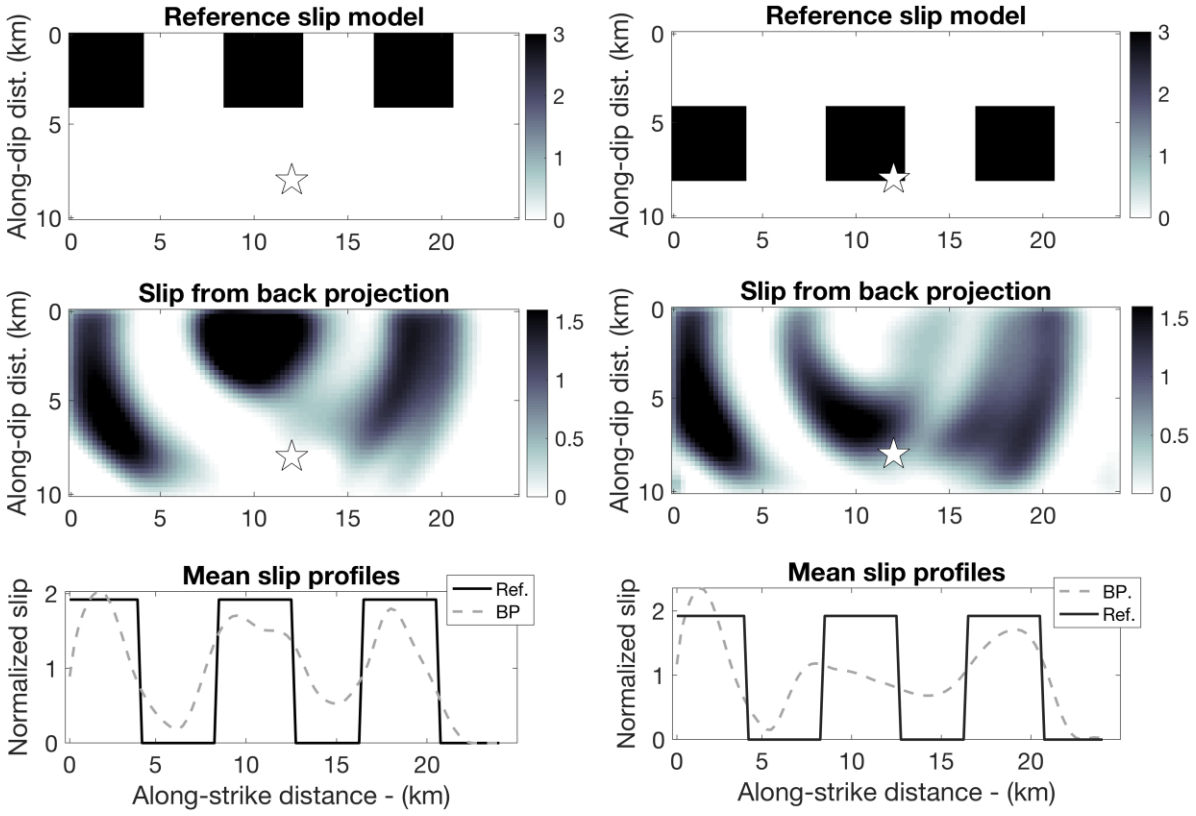

Figure 5: Resolution test of the isochrones backprojection technique. Synthetic ASTFs are generated using two reference slip models (top) at the stations for which ASTFs have been inferred from the seismological data (represented on Figure 1 in red and green), assuming a rupture velocity of 2 km/s and a hypocenter at 7.8 km depth. Middle and bottom figures show the inferred slip maps and slip profiles averaged over the fault dip, respectively.

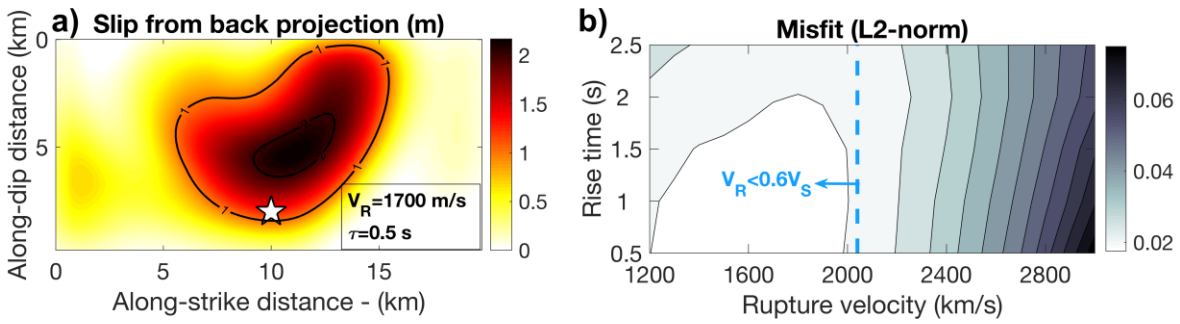

Figure 6: Results from the isochrone backprojection technique for the M_w6.4 Petrinja earthquake. a) Slip map obtained from the isochrone backprojection of ASTFs, assuming a hypocentre at 7.8 km. The minimum misfit between synthetic and observed ASTFs is obtained for a rupture velocity of 1.7 km/s and a rise time of 0.5 s. b) Misfit value as a function of rise time and rupture velocity.

3.2 Bayesian Kinematic Inversion of ASTFs

Next, we derive the 2020 Petrinja earthquake rupture model following a two-stage Bayesian inversion procedure detailed in Causse et al. (2017). The adopted inversion technique seeks to reduce the number of inverted parameters and identify only robust key features of the rupture propagation. ASTFs are inverted to obtain spatio-temporal rupture parameters, including mean rupture velocity, mean rise time and slip distribution relative to the hypocenter. By aligning slip distribution with independently analyzed epicentral location and hypocentral depth, we then establish absolute slip distribution. This method is suitable for moderate-magnitude events, for which ASTFs might be affected by significant noise (Convertito et al., 2021). The initial stage involves identifying the "best" rupture model (i.e. the maximum likelihood model). The second stage explores a range of "good" models (i.e. acceptable given the model uncertainty), from which uncertainty on the rupture parameters is quantified, including for instance trade-off between rupture parameters.

Figure 7 illustrates the expected tradeoffs between parameters in the case of a simple bilateral line source. Apparent source duration depends on rupture length (L), rupture velocity (V_R), and rise time (τ) for stations perpendicular to the rupture direction and depends also on phase velocity (c) for the other directions of observation. While a good azimuthal coverage combining seismological data recorded along and perpendicular to the fault can resolve L in bilateral ruptures, there is a trade-off between V_R and τ.

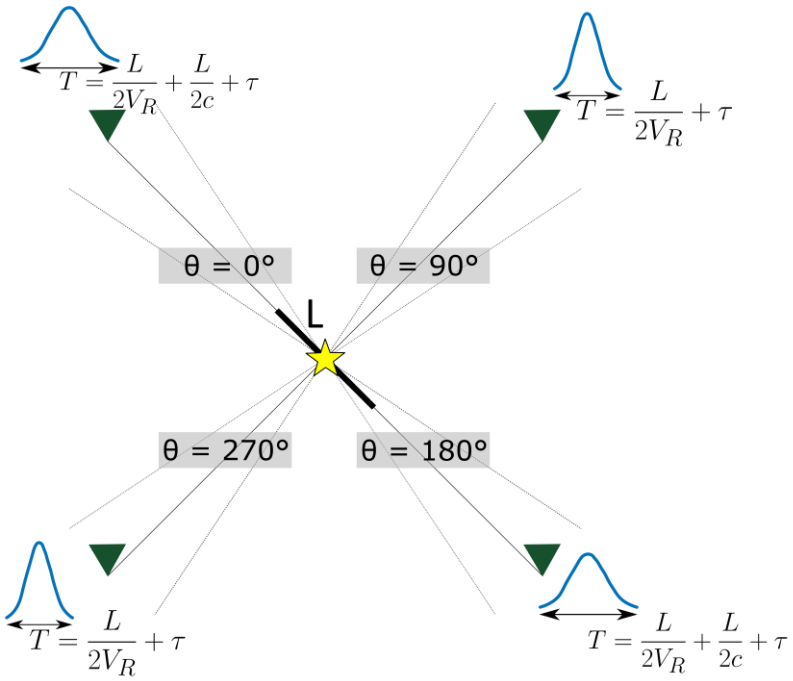

Figure 7. Theoretical value of the apparent source duration (T) for a line source rupturing bilaterally at rupture velocity V_R, for several source-receiver azimuths θ. τ represents the rise time.

3.2.1 Inversion procedure

We limit the fault dimensions to a length of 20,000 meters and a width of 8,000 meters, considering the shallow hypocentral depth (Baize et al., 2022). We assume a subvertical fault with a dip of 84° and divide the fault plane into subfaults of 500 m x 500 m. At this stage, we assign equal weights to all data. Additionally, to convert seismic moment into slip, we use rigidity value as $\mu = 3.5 \times 10^{10}$ Pa. McGarr & Fletcher (2003) predict a maximum slip of ~2.5 m for a M_W6.4 event. To allow for potentially large slip, we then set the maximum slip value to 6 m. As we anticipate lower resolution for V_R and τ, we consider relatively broad parameter ranges, with V_R between 800 m/s and 4000 m/s and τ between 0.75 s and 3 s (based on an expected average value of 1.5 s for a M_W6.4 earthquake with uncertainty factor of ~2, Gusev and Chebrov, 2019). In addition, we use a Love wave phase velocity of 3500 m/s (Supplementary material S4). Finally, we keep the nucleation point position on the fault plane as a free parameter.

In this study, we adopt the concept of a self-adapting grid (e.g. Causse et al., 2017; Hallo & Gallovic 2020). The slip values are then not inverted on a regular grid of points but at a few control points, whose location is also inverted. The chosen number of these points enables to control the spatial complexity actually required by the data. After obtaining slip values at these control points, the overall slip is interpolated over the fault plane using spline interpolation, setting slip to zero on the fault edges (Causse et al., 2017). Here, four control points are used. We have tested that using more control points does not improve the fit with ASTFs. Note that our inversion code can also identify potential variations

of rupture velocity by incorporating control points that define local rupture velocity. Nevertheless, we have checked that using up to 4 control points does not result in a better fit with ASTF (Supplementary material S5). In the following, we then assume constant rupture velocity. The rise time is also assumed to be constant over the fault plane.

To explore the model space, we employ a Markov chain using the Metropolis algorithm (Metropolis et al., 1953). This iterative approach is simply a random walk, in which the "bad" models are unlikely to be accepted (e.g. Causse et al., 2017). The likelihood function is assumed to be Gaussian:

$$f(\boldsymbol{d}|\boldsymbol{m}) = c \cdot exp\left(\frac{-|\boldsymbol{d}-\boldsymbol{g}(\boldsymbol{m})|^2}{2\sigma^2}\right), \quad (4)$$

where $\boldsymbol{d}$ and $\boldsymbol{m}$ represent the data and model space, respectively, $\boldsymbol{g}$ represents the forward model to generate ASTFs from the rupture parameters and σ is a scalar. During the walk, a new candidate $\boldsymbol{m}_i$ at iteration i is accepted if the ratio of the likelihood functions $p=f(\boldsymbol{d}|\boldsymbol{m}_i)/f(\boldsymbol{d}|\boldsymbol{m}_{i-1})$ returns a probability larger than a random number between 0 and 1. p is expressed as:

$$p = \frac{f(\boldsymbol{d}|\boldsymbol{m_i})}{f(\boldsymbol{d}|\boldsymbol{m_{i-1}})} = exp\left(\frac{|\boldsymbol{d}-\boldsymbol{g}(\boldsymbol{m_{i-1}})|^2-|\boldsymbol{d}-\boldsymbol{g}(\boldsymbol{m_i})|^2}{2\sigma^2}\right) \quad (5)$$

so that the acceptance rate of new candidates decreases with decreasing values of σ.

In the initial stage, our aim is to find the global minimum of the cost function by using a simulated annealing (SA) cooling scheme (Kirkpatrick et al., 1983). This involves an exploration of the model space followed by a gradual reduction of the σ values. To obtain the maximum likelihood model (the so-called "best" model), we conducted 14,000 iterations (Supplementary Figure S6).

3.2.2 Inversion result

We use this inversion procedure together with ASTFs obtained with f_{max}=0.5Hz (section 2.2) to obtain a source model. The best source model is depicted in Figure 8. The effective rupture length (L_{eff}) and effective rupture width (W_{eff}) are computed as the maximum dimensions in the along-strike and along-dip directions for which slip values exceed 1 meter. The simulated ASTFs from our preferred model accurately describe the observed ASTFs, with a global level of fit, computed as the mean value of the coefficient of determination R^2 for each station, above 90% (Figure 9 and Supplementary material S5).

The best model indicates a very slow rupture velocity (~0.4V_S), significant maximum slip value of about 6 m, and relatively small rupture dimensions. The single slip patch, with slip values above 1 m, has an effective length of 6.5 km and an effective width of 6 km. It is located above the nucleation point, resulting in predominantly upward rupture propagation, which is reported by Herak & Herak (2023)

as well. The maximum slip area is however located slightly to the southeast of the nucleation, indicating a more southeast rupture propagation. Moreover, our obtained slip peaked approximately 3 km above the nucleation point and at an approximate depth of 4 - 5 km. For comparison, Herak & Herak (2023) reported an average slip patch of dimensions 5 km × 4 km located 4 km above the nucleation point with a peak slip of ~4 m based on the Kastelic et al. (2021) source model obtained from InSAR data. Xiong et al. (2022) also derived a source model using InSAR data suggesting an 8.33 km × 5.40 km slip patch with a maximum slip of 3.5 m. Interestingly, Henriquet et al. (2022) obtained a source model using a benchmark network combined with GNSS data describing a two-patch rupture 18 km long and 7 km wide. By its position and size, the slip patch of our best model mostly agrees with their deeper 7 km × 5 km slip patch despite its maximum slip being 3.5 m.

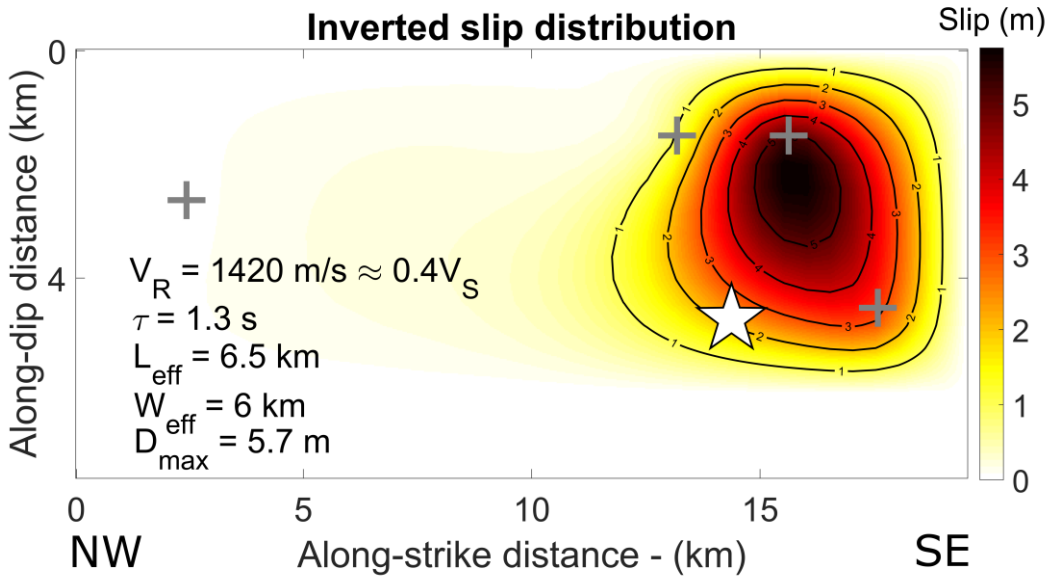

Figure 8. Finite source model obtained from ASTFs kinematic inversion. The color-scale depicts the final slip along the strike (NW-SE) and dip of the Pokupsko fault relative to the nucleation point represented by the white star. Grey crosses indicate the final locations of the four control points used to define the slip distribution.

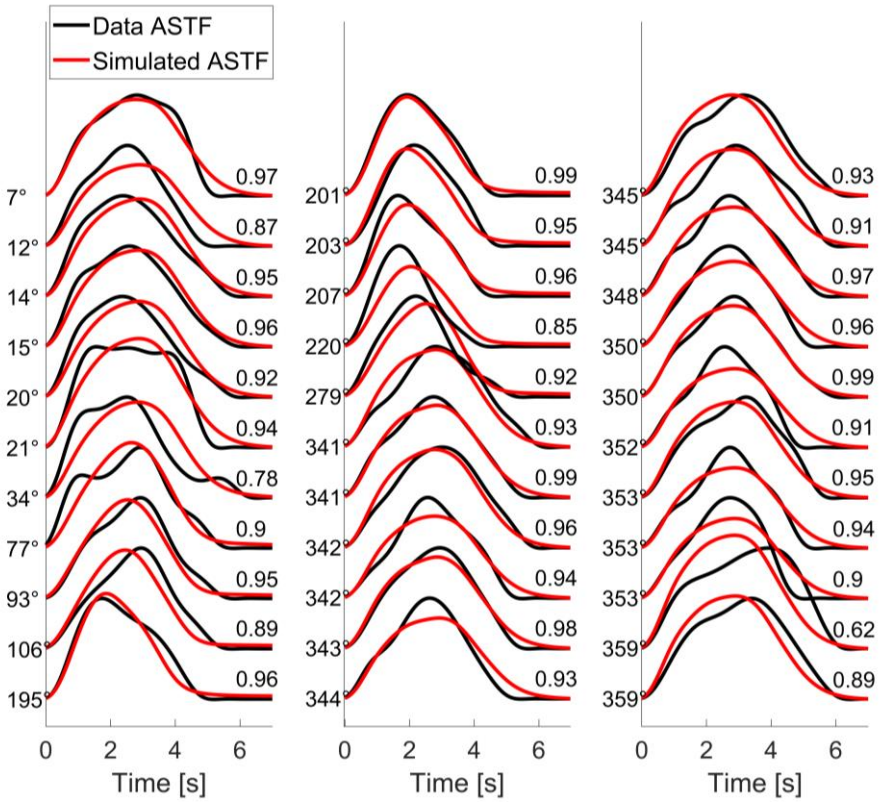

403

404 **Figure 9.** Comparison between apparent source time functions obtained from Love waves lowpass
405 filtered at f_{max}=0.5 Hz (black) and simulated synthetic functions (red). Source-to-station azimuths are
406 indicated next to the left axis and the level of fit is indicated on right side. The azimuth is 0° along the
407 fault to the northwest.

408

409 3.2.3 Uncertainty analysis

410

411 We here aim to derive the posterior distribution of the obtained kinematic parameters, representing
412 a population of rupture models that all result in an acceptable fit with the data. Analyzing this model
413 population offers insights into model resolution and potential parameter trade-offs. In this second
414 stage, we use the results of the best model from the first stage as the initial parameter guess, exploring
415 the model space starting from this point. The initial condition for the acceptable error (σ^2) is set as the
416 cost value of the best model from the first stage. To mitigate the impact of uneven azimuthal coverage,
417 σ^2 is determined as the squared median value of cost values for source-to-receiver azimuthal classes
418 computed every 45°. In this stage we perform 100,000 iterations, selecting every 100th sample to
419 avoid autocorrelation, resulting in the 10,000 samples representing posterior distribution of kinematic
420 source parameters (Figure 10).

From the posterior distributions we observe well-constrained rupture dimension and maximum slip, contrary to rupture velocity and rise time, which display expected uncertainties. The correlation matrix (Figure 11) illustrates the trade-off between rupture velocity (V_R) and rise time (τ), resulting in decreased resolution for V_R. Despite these trade-offs, the inversion suggests a slow rupture propagation ($V_R < 0.6\ V_S$), where V_S = 3400 m/s denotes the shear wave velocity at the rupture depth from the Balkan velocity model (B.C.I.S., 1972). The V_R values are approximately normally distributed with mean 1790 m/s and standard deviation ~330 m/s. Moreover, the rise time is very poorly constrained. Note however that the value of 1.3 s obtained from the best model with maximum likelihood agrees with past earthquake analyses reporting an average rise time of ~1.5 s for a M_W6.4 earthquake (Gusev and Chebrov, 2019).

Additionally, we conducted several tests to assess the sensitivity of our model to the initial input parameters (Supplementary material S5). We inspected the impact of: (1) ASTF processing (original or convolved with a 0.7 s Boxcar function as explained in the section 2.3, low-pass filtering at 0.1 Hz or 0.5 Hz); (2) station weights; (3) fixed or free nucleation position; (4) phase velocity values; (5) control points to account for rupture velocity variability over the fault plane. All tested scenarios indicate the same tendency as the best model: slow rupture velocity ($<0.6V_S$), relatively small slip patch, and significant maximum slip value. As expected, the most impacted parameter is the rise time, which is from far the least resolved.

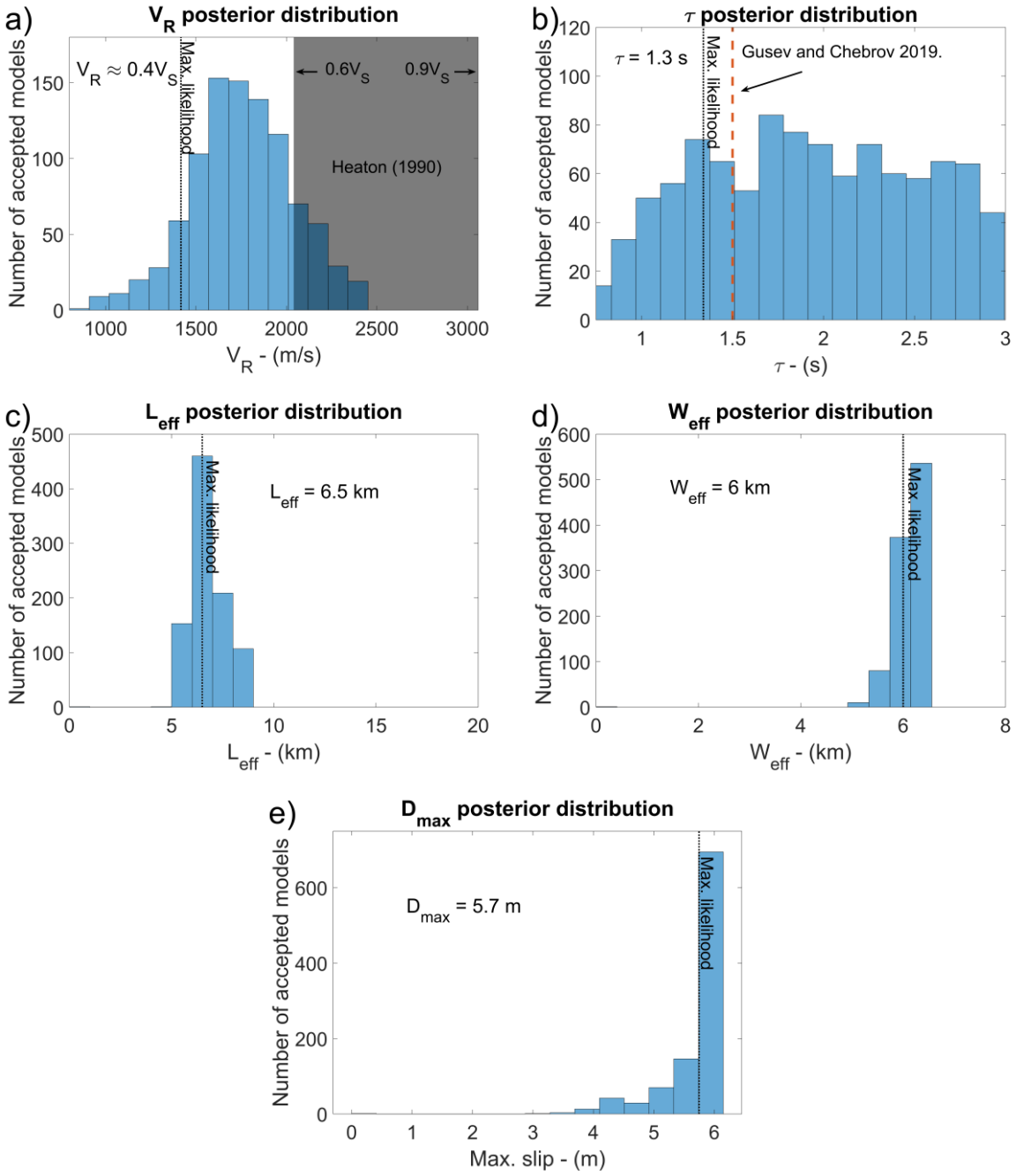

Figure 10. Posterior marginal distributions of obtained physical rupture parameters represented by histograms: a) average rupture velocity (the grey area represents the range of values reported by Heaton (1990); b) rise time (the dashed red line represents the median rise time value reported by Gusev and Chebrov (2019) for a M_w6.4 earthquake; c) effective rupture length; d) effective rupture width; e) maximum slip. The maximum likelihood values are represented with the black dashed line.

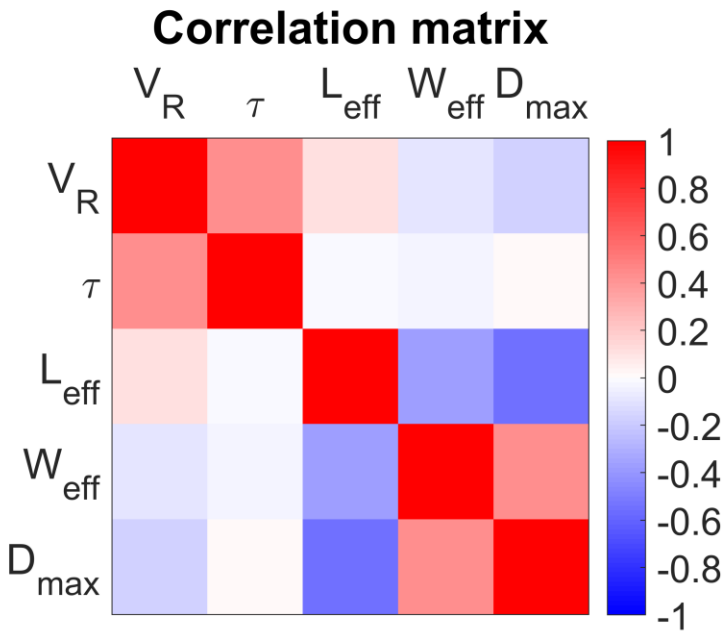

Figure 11. Correlation matrix of rupture parameters obtained from the Bayesian kinematic inversion.

4. Discussion

The 2020 Petrinja earthquake is a rare example of shallow rupture with large stress drop (~25 MPa). The large stress drop suggests that the fault strength was large enough to allow strong accumulation and then release of stress. Such conditions are favored by geometric complexity and strength heterogeneity of the fault (e.g. Madariaga, 1979; Fang and Dunham, 2013; Zielke et al., 2017), features expected for an immature and complex fault system like the Petrinja-Pokupsko fault (Xiong et al., 2021). The long recurrence interval of large earthquakes on this fault, characterized by slip rate estimates of 0.1-0.6 mm/yr (Basili et al., 2013; Baize et al., 2022) could also promote cohesion recovery and increase fault strength (Xu et al., 2023).

Furthermore, the high seismological stress drop is consistent with the small rupture length (~7 km) and the large maximum slip that probably reached over 5 m at 4-5 km depth. Surface rupture observations indicate maximum surface slip of only 38 cm (Baize et al., 2022), which implies a large shallow slip deficit. Large deficit is also revealed by the slip distribution obtained from geodetic data (Henriquet et al., 2022). Observations of shallow slip deficit are commonly attributed to shallow distributed inelastic deformation in an immature fault context (Fialko et al., 2005; Dolan and Haravitch, 2014; Roten et al., 2017; Li et al., 2020). Shallow coseismic deformation during the Petrinja earthquake may have occurred in a zone of diffuse deformation (or damage zone) a few kilometers wide as revealed by the 'flower structure' of the Petrinja-Pokupsko fault and by the segmented

coseismic rupture observed at the surface (Baize et al., 2022). The broad extent of the aftershock distribution of the Petrinja seismic sequence (Figure 1) is also a characteristic of immature fault systems and distributed coseismic deformation (Perrin et al., 2021).

Another unusual characteristic of the 2020 Petrinja earthquake is its slow rupture. The rupture propagated at a speed of about $0.5V_S$, while commonly reported rupture speeds range between ~$0.6V_S$ and ~$0.9V_S$ (e.g. Heaton, 1990; Somerville et al. 1999). Low rupture speeds have been observed for other continental intraplate earthquakes generally on immature faults structures with complex geometries, including the 1999 Hector Mine (Kaverina, 2002), the 2012 M_W5.8 and M_W6.0 Emilia (Causse et al., 2017; Convertito et al., 2021), the 2016 Tottori (Ross et al., 2018), the 2020 Elazig (Pousse-Beltran et al., 2020), the 2021 Ridgecrest (Liu et al., 2019; Goldberg et al., 2020) and the 2021 Yangbi, Yunnan (Gong et al., 2022) earthquakes. Slow rupture implies strong energy dissipation in the fault zone near the crack tip and in the surrounding rock. Processes of energy dissipation during faulting include off-fault cracking (Andrews, 2005; Rice et al., 2005) and thermal processes such as melting and thermal-pressurization (Rice, 2006). Nonelastic dynamic simulations shows that off-fault cracking reduces rupture velocity (Andrews 2005; Gabriel et al., 2013). It is likely that off-fault cracking in the immature and segmented Pertinja-Pokupsko fault zone strongly contributed to the low rupture velocity.

In terms of earthquake energy partitioning, slow rupture propagation implies that a relatively small amount of the available energy is radiated as seismic waves (*i.e*. lower radiation efficiency) (Freund, 1972; Venkataraman and Kanamori, 2004; Kanamori and Rivera, 2006). An interesting question is whether low rupture velocity and radiation efficiency together with a large stress drop are common features of earthquake ruptures. In other words, does the energy dissipated during the rupture process increase with stress drop? Such properties have been reported for the 2016 M_W6.2 Tottori earthquake (V_R~0.5-0.6V_S, η_R~7%, $\Delta\tau$~20-30 MPa) (Ross et al., 2018). At a global scale, Chounet et al. (2018) documented rupture properties of 96 shallow earthquakes with magnitude M_W from 6 to 9 and show that rupture velocity and stress drop are anticorrelated, supporting slower rupture propagation when stress drop is large. Another example where this behavior is explicitly mentioned is the 2003 Big Bear sequence for events with magnitude 3-4 (Tan and Helmberger, 2010). Anticorrelation between rupture velocity and stress drop was initially proposed by Causse and Song (2015) by combining observations of the variability of source properties and high-frequency ground motion. Dynamic rupture simulations and laboratory experiments conducted in homogeneous media generally indicate a positive correlation between rupture velocity and stress drop (e.g. Andrews, 1976; Guatteri, 2004; Dong et al., 2023). However, dynamic simulations including off-fault plasticity show that this trend can be reversed, depending on the orientation of the maximum compressive stress

angle with respect to fault strike (denoted ψ) (Gabriel et al., 2013). Such a behavior is observed for ψ values larger than 50°. In this case, off-fault energy dissipation is strongly boosted as stress drop is increased. Stress orientations based on focal mechanism in the Petrinja region oscillate around the N-S axis (Herak et al., 2009; Baize et al., 2022), in agreement with geodetic velocity field (Métois et al., 2015). This leads to ψ values of ~60-65° for the Petrinja-Pokupsko fault - consistently with the transpressive faulting regime, supporting strong off-fault energy dissipation enhanced by the large stress drop. In other words, high stress drop may be counterproductive for earthquake rupture because energy dissipation in the surrounding material becomes catastrophic, which in turn makes the rupture on the main fault less efficient. Further studies should investigate if large stress drop and slow rupture velocity are observed in similar tectonic environments. Another interpretation is that rupture may appear to be slow because it is confined to a small fault zone due to the geometric complexity and strength heterogeneity of the immature fault, conditions also responsible for high stress drop. This is an interesting question for future rupture dynamic studies.

Finally, an important question for seismic hazard assessment is the implication of such rupture properties on ground motion. Unfortunately, the strong ground motion of the Petrinja earthquake was not recorded at less than ~50 km from the source. Radiguet et al. (2009) observed that ground motions generated on immature faults are ~1.5 time larger than the ones on mature faults. The large seismological stress drop that we obtain for the Petrinja-Pokupsko immature fault (~25 MPa) suggests that the high-frequency ground motion was high, at least in the region far from the source (e.g. Cotton et al., 2013). Near-fault ground motion is however highly sensitive to the rupture velocity (e.g. Bouchon et al., 2006; Fayjaloun et al., 2020). Further studies are necessary to quantify the near-fault ground motion and analyze the impact of the large stress drop and slow rupture propagation.

5. Conclusions

In this study, we analyzed the rupture process of the December 29th, 2020, M_W6.4 earthquake that struck the wider Petrinja area (Croatia) using seismological data from more than 80 broadband stations. We used an EGF deconvolution method to compute stress drop and to derive ASTFs. Using two separate methods, Bayesian inversion of ASTFs and backprojection of ASTFs on isochrones, we derived a kinematic rupture model. Both methods revealed a relatively small rupture length of less than 10 km and a significant maximum slip of more than 5 m, consistent with the large Brune's stress drop (~25 MPa) and the relatively short rupture duration (~5 s). Moreover, the two methods unambiguously point to a slow rupture velocity of 40-60% of the shear wave velocity.

The Petrinja earthquake is a rare example of shallow event with large stress drop. The large stress drop may have been favored by the complexity and heterogeneity of the fault geometry, which are typical features of immature fault systems. While dynamic rupture simulations and laboratory experiments commonly indicate that rupture velocity increases with stress drop, the rupture propagation during the Petrinja rupture was particularly slow. Such particular behavior is supported by anticorrelation between stress drop and rupture velocity observed in set of rupture models (Causse et al., 2015; Chounet et al., 2018). Physically, the slow rupture velocity may be explained by a particularly strong energy dissipation in off-fault cracking, enhanced by the large stress drop, as reported in some dynamic rupture simulations including off-fault plasticity. Whether or not large stress drop and slow rupture propagation are common features of earthquakes in immature intraplate setting prompts further investigations. An important question for seismic hazard assessment is also how these particular rupture properties affect near-fault ground motion.

Acknowledgements

This work has been supported by the Norwegian Financial Mechanism 2014-2021 under the project "Investigation of seismically vulnerable areas in Croatia and seismic ground motion assessment - CRONOS", 04-UBS-U-0002/22-90, Croatian Science Foundation (HRZZ) Research Project „Seismic risk assessment of cultural heritage buildings in Croatia – SeisRICHerCRO", IP-2020-02-3531, and „SH-CROCO Seismic Hazard in CROatia: a COllaborative approach" project. This work was also supported by program TelluS of the Institut National des Sciences de l'Univers (SH-CROCO project). We also thank T.M. Mitchell for fruitful discussions. We would like to thank Croatian Seismological Survey for providing us with the seismicity data within the Croatian Earthquake Catalogue. Finally, we are grateful to the ORFEUS data center where the European data has been retrieved.

Data availability

Seismological data across Europe are available in open-access at the Observatories and Research Facilities for European Seismology (ORFEUS) data center. They have been downloaded using webservices of the European Integrated Data Archive (EIDA, https://www.orfeus-eu.org/data/eida/webservices/) and ObsPy codes. The Croatian data that support the findings of this study are available from the corresponding author, [IL], upon reasonable request.

References

Abercrombie, R. E. (2015). Investigating uncertainties in empirical Green's function analysis of earthquake source parameters. *Journal of Geophysical Research: Solid Earth*, *120*(6), 4263–4277. https://doi.org/10.1002/2015jb011984

569 Abercrombie, R. E., Bannister, S., Ristau, J., & Doser, D. (2016). Variability of earthquake stress drop in
570 a subduction setting, the Hikurangi Margin, New Zealand. *Geophysical Journal International*,
571 *208*(1), 306–320. https://doi.org/10.1093/gji/ggw393

572 Aki, K. (1967). Scaling law of seismic spectrum. *Journal of Geophysical Research*, *72*(4), 1217–1231.
573 https://doi.org/10.1029/jz072i004p01217

574 Allmann, B. P., & Shearer, P. M. (2009). Global variations of stress drop for moderate to large
575 earthquakes. *Journal of Geophysical Research: Solid Earth*, *114*(B1).
576 https://doi.org/10.1029/2008jb005821

577 Anderson, H., & Jackson, J. (1987). Active tectonics of the Adriatic Region. *Geophysical Journal*
578 *International*, *91*(3), 937–983. https://doi.org/10.1111/j.1365-246x.1987.tb01675.x

579 Andrews, D. J. (1976). Rupture propagation with finite stress in antiplane strain. *Journal of Geophysical*
580 *Research*, *81*(20), 3575–3582. https://doi.org/10.1029/jb081i020p03575

581 Andrews, D. J. (2005). Rupture dynamics with energy loss outside the slip zone. *Journal of Geophysical*
582 *Research: Solid Earth*, *110*(B1). https://doi.org/10.1029/2004jb003191

583 Baize, S., Amoroso, S., Belić, N., Benedetti, L., Boncio, P., Budić, M., Cinti, F. R., Henriquet, M.,
584 Jamšek Rupnik, P., Kordić, B., Markušić, S., Minarelli, L., Pantosti, D., Pucci, S., Špelić, M., Testa,
585 A., Valkaniotis, S., Vukovski, M., Atanackov, J., … Ricci, T. (2022). Environmental effects and
586 seismogenic source characterization of the December 2020 earthquake sequence near Petrinja,
587 Croatia. *Geophysical Journal International*, *230*(2), 1394–1418.
588 https://doi.org/10.1093/gji/ggac123

589 Battaglia, M., Murray, M. H., Serpelloni, E., & Bürgmann, R. (2004). The Adriatic region: An
590 independent microplate within the Africa-Eurasia collision zone. *Geophysical Research Letters*,
591 *31*(9). https://doi.org/10.1029/2004gl019723

592 B.C.I.S. (1972): Tables des temp de propagation des ondes séismiques (Hodochrones) pour la region
593 des Balkans, Manuel d'utilisation, Bureau Central International de Séismologie, Strasbourg.

594 Beroza, G. C., & Spudich, P. (1988). Linearized inversion for fault rupture behavior: Application to the
595 1984 Morgan Hill, California, earthquake. *Journal of Geophysical Research: Solid Earth*, *93*(B6),
596 6275–6296. https://doi.org/10.1029/jb093ib06p06275

597 Bertero, M., Bindi, D., Boccacci, P., Cattaneo, M., Eva, C., & Lanza, V. (1997). Application of the
598 projected Landweber method to the estimation of the source time function in seismology.
599 *Inverse Problems*, *13*(2), 465–486. https://doi.org/10.1088/0266-5611/13/2/017

600 Bouchon, M., Hatzfeld, D., Jackson, J. A., & Haghshenas, E. (2006). Some insight on why Bam (Iran) was
601 destroyed by an earthquake of relatively moderate size. *Geophysical Research Letters*, *33*(9).
602 https://doi.org/10.1029/2006gl025906

603 Brune, J. N. (1970). Tectonic stress and the spectra of seismic shear waves from earthquakes. *Journal*
604 *of Geophysical Research*, *75*(26), 4997–5009. https://doi.org/10.1029/jb075i026p04997

605 Calais, E., Nocquet, J.-M., Jouanne, F., & Tardy, M. (2002). Current strain regime in the Western Alps
606 from continuous Global Positioning System measurements, 1996–2001. *Geology*, *30*(7), 651.
607 https://doi.org/10.1130/0091-7613(2002)030<0651:csritw>2.0.co;2

608 Causse, M., Cornou, C., Maufroy, E., Grasso, J.-R., Baillet, L., & El Haber, E. (2021). Exceptional ground
609 motion during the shallow Mw 4.9 2019 Le Teil earthquake, France. *Communications Earth*
610 *& Environment*, *2*(1). https://doi.org/10.1038/s43247-020-00089-0

611 Causse, M., Cultrera, G., Moreau, L., Herrero, A., Schiappapietra, E., & Courboulex, F. (2017). Bayesian
612 rupture imaging in a complex medium: The 29 May 2012 Emilia, Northern Italy, earthquake.
613 *Geophysical Research Letters*, *44*(15), 7783–7792. https://doi.org/10.1002/2017gl074698

614 Causse, M., & Song, S. G. (2015). Are stress drop and rupture velocity of earthquakes independent?
615 Insight from observed ground motion variability. *Geophysical Research Letters*, *42*(18), 7383–
616 7389. https://doi.org/10.1002/2015gl064793

617 Chounet, A., Vallée, M., Causse, M., & Courboulex, F. (2018). Global catalog of earthquake rupture
618 velocities shows anticorrelation between stress drop and rupture velocity. *Tectonophysics*, *733*,
619 148–158. https://doi.org/10.1016/j.tecto.2017.11.005

620 Convertito, V., Pino, N. A., & Piccinini, D. (2021). Concentrated slip and low rupture velocity for the
621 may 20, 2012, MW 5.8, Po plain (northern italy) earthquake revealed from the analysis of source
622 time functions. *Journal of Geophysical Research: Solid Earth*, *126*(1).
623 https://doi.org/10.1029/2019jb019154

624 Cotton, F., Archuleta, R., & Causse, M. (2013). What is Sigma of the Stress Drop? *Seismological*
625 *Research Letters*, *84*(1), 42–48. https://doi.org/10.1785/0220120087

626 Courboulex, F., Vallée, M., Causse, M., & Chounet, A. (2016). Stress-Drop variability of shallow
627 earthquakes extracted from a global database of source time functions. *Seismological Research*
628 *Letters*, *87*(4), 912–918. https://doi.org/10.1785/0220150283

629 Dolan, J. F., & Haravitch, B. D. (2014). How well do surface slip measurements track slip at depth in
630 large strike-slip earthquakes? The importance of fault structural maturity in controlling on-fault
631 slip versus off-fault surface deformation. *Earth and Planetary Science Letters*, *388*, 38–47.
632 https://doi.org/10.1016/j.epsl.2013.11.043

633 Dong, P., Xia, K., Xu, Y., Elsworth, D., & Ampuero, J.-P. (2023). Laboratory earthquakes decipher control
634 and stability of rupture speeds. *Nature Communications*, *14*(1).
635 https://doi.org/10.1038/s41467-023-38137-w

636 Eshelby, J. D. (1957). The determination of the elastic field of an ellipsoidal inclusion, and related
637 problems. *Proceedings of the Royal Society of London. Series A. Mathematical and Physical*
638 *Sciences*, *241*(1226), 376–396. https://doi.org/10.1098/rspa.1957.0133

639 Fang, Z., & Dunham, E. M. (2013). Additional shear resistance from fault roughness and stress levels
640 on geometrically complex faults. *Journal of Geophysical Research: Solid Earth*, *118*(7), 3642–
641 3654. https://doi.org/10.1002/jgrb.50262

642 Fayjaloun, R., Causse, M., Cornou, C., Voisin, C., & Song, S. G. (2019). Sensitivity of high-frequency
643 ground motion to kinematic source parameters. *Pure and Applied Geophysics*, *177*(5), 1947–
644 1967. https://doi.org/10.1007/s00024-019-02195-3

645 Festa, G., & Zollo, A. (2006). Fault slip and rupture velocity inversion by isochrone backprojection.
646 *Geophysical Journal International*, *166*(2), 745–756. https://doi.org/10.1111/j.1365-
647 246x.2006.03045.x

648 Fialko, Y., Sandwell, D., Simons, M., & Rosen, P. (2005). Three-dimensional deformation caused by the
649 Bam, Iran, earthquake and the origin of shallow slip deficit. *Nature*, *435*(7040), 295–299.
650 https://doi.org/10.1038/nature03425

651 Freund, L. B. (1972). Crack propagation in an elastic solid subjected to general loading—I. Constant
652 rate of extension. *Journal of the Mechanics and Physics of Solids*, *20*(3), 129–140.

https://doi.org/10.1016/0022-5096(72)90006-3

Gabriel, A. -a., Ampuero, J. -p., Dalguer, L. A., & Mai, P. M. (2013). Source properties of dynamic rupture pulses with off-fault plasticity. *Journal of Geophysical Research: Solid Earth*, *118*(8), 4117–4126. https://doi.org/10.1002/jgrb.50213

Goldberg, D., Melgar, D., Thomas, A., Sahakian, V., Xu, X., Geng, J., & Crowell, B. (2019). *Complex rupture of an immature fault zone: A simultaneous kinematic model of the 2019 Ridgecrest, CA earthquakes*. California Digital Library (CDL). http://dx.doi.org/10.31223/osf.io/s79bk

Gong, W., Ye, L., Qiu, Y., Lay, T., & Kanamori, H. (2022). Rupture directivity of the 2021MW6.0 Yangbi, Yunnan earthquake. *Journal of Geophysical Research: Solid Earth*, *127*(9). https://doi.org/10.1029/2022jb024321

Guatteri, M. (2004). A pseudo-dynamic approximation to dynamic rupture models for strong ground motion prediction. *Bulletin of the Seismological Society of America*, *94*(6), 2051–2063. https://doi.org/10.1785/0120040037

Gusev, A. A., & Chebrov, D. (2019). On scaling of earthquake rise-time estimates. *Bulletin of the Seismological Society of America*, *109*(6), 2741–2745. https://doi.org/10.1785/0120180214

Hallo, M., & Gallovič, F. (2020). Bayesian self-adapting fault slip inversion with green's functions uncertainty and application on the 2016 Mw7.1 Kumamoto Earthquake. *Journal of Geophysical Research: Solid Earth*, *125*(3). https://doi.org/10.1029/2019jb018703

Heaton, T. H. (1990). Evidence for and implications of self-healing pulses of slip in earthquake rupture. *Physics of the Earth and Planetary Interiors*, *64*(1), 1–20. https://doi.org/10.1016/0031-9201(90)90002-f

Henriquet, M., Kordic, B., Métois, M., Lasserre, C., Baize, S., Benedetti, L., Spelić, M., & Vukovski, M. (2022). Rapid remeasure of dense civilian networks as a game-changer tool for surface deformation monitoring: The case study of the Mw 6.4 2020 Petrinja Earthquake, Croatia. *Geophysical Research Letters*, *49*(24). https://doi.org/10.1029/2022gl100166

Herak, D., & Herak, M. (2010). The kupa valley (croatia) earthquake of 8 october 1909--100 years later. *Seismological Research Letters*, *81*(1), 30–36. https://doi.org/10.1785/gssrl.81.1.30

Herak, D., Herak, M., & Tomljenović, B. (2009). Seismicity and earthquake focal mechanisms in North-Western Croatia. *Tectonophysics*, *465*(1–4), 212–220. https://doi.org/10.1016/j.tecto.2008.12.005

Herak, M., & Herak, D. (2023). Properties of the Petrinja (Croatia) earthquake sequence of 2020–2021 – Results of seismological research for the first six months of activity. *Tectonophysics*, *858*, 229885. https://doi.org/10.1016/j.tecto.2023.229885

Herak, M., Herak, D., & Markušić, S. (1996). Revision of the earthquake catalogue and seismicity of Croatia, 1908–1992. *Terra Nova*, *8*(1), 86–94. https://doi.org/10.1111/j.1365-3121.1996.tb00728.x

Houston, H. (2001). Influence of depth, focal mechanism, and tectonic setting on the shape and duration of earthquake source time functions. *Journal of Geophysical Research: Solid Earth*, *106*(B6), 11137–11150. https://doi.org/10.1029/2000jb900468

Kanamori, H., & Rivera, L. (2006). Energy partitioning during an earthquake. In *Earthquakes: Radiated Energy and the Physics of Faulting* (pp. 3–13). American Geophysical Union. http://dx.doi.org/10.1029/170gm03

695 Kane, D. L., Prieto, G. A., Vernon, F. L., & Shearer, P. M. (2011). Quantifying seismic source parameter
696 uncertainties. *Bulletin of the Seismological Society of America*, *101*(2), 535–543.
697 https://doi.org/10.1785/0120100166

698 Kastelic, V., Atzori, S., Carafa, M. M. C., Marin Govorčin, M., Herak, D., Herak, M., Matoš, B., Stipčević,
699 J., & Bruno Tomljenović, B. (2021). *Petrinja Seismogenic Source and its 2020-2021 Earthquake*
700 *Sequence (central Croatia)*. Copernicus GmbH. http://dx.doi.org/10.5194/egusphere-egu21-
701 16585

702 Kaverina, A. (2002). The combined inversion of seismic and geodetic data for the source process of
703 the 16 october 1999 Mw 7.1 Hector Mine, California, earthquake. *Bulletin of the Seismological*
704 *Society of America*, *92*(4), 1266–1280. https://doi.org/10.1785/0120000907

705 Király-Proag, E., Satriano, C., Bernard, P., & Wiemer, S. (2019). Rupture process of the Mw 3.3
706 Earthquake in the St. Gallen 2013 Geothermal Reservoir, Switzerland. *Geophysical Research*
707 *Letters*, *46*(14), 7990–7999. https://doi.org/10.1029/2019gl082911

708 Kirkpatrick, S., Gelatt, C. D., Jr., & Vecchi, M. P. (1983). Optimization by simulated annealing. *Science*,
709 *220*(4598), 671–680. https://doi.org/10.1126/science.220.4598.671

710 Lay, T., & Wallace, T. C. (1995). *Modern global seismology*. Elsevier.

711 Li, Y., Bürgmann, R., & Zhao, B. (2020). Evidence of fault immaturity from shallow slip deficit and lack
712 of postseismic deformation of the 2017 Mw 6.5 Jiuzhaigou Earthquake. *Bulletin of the*
713 *Seismological Society of America*, *110*(1), 154–165. https://doi.org/10.1785/0120190162

714 Liu, C., Lay, T., Brodsky, E. E., Dascher-Cousineau, K., & Xiong, X. (2019). Coseismic rupture process of
715 the large 2019 ridgecrest earthquakes from joint inversion of geodetic and seismological
716 observations. *Geophysical Research Letters*, *46*(21), 11820–11829.
717 https://doi.org/10.1029/2019gl084949

718 Madariaga, R. (1976). Dynamics of an expanding circular fault. *Bulletin of the Seismological Society of*
719 *America*, *66*(3), 639–666. https://doi.org/10.1785/bssa0660030639

720 Madariaga, R. (1979). On the relation between seismic moment and stress drop in the presence of
721 stress and strength heterogeneity. *Journal of Geophysical Research: Solid Earth*, *84*(B5), 2243–
722 2250. https://doi.org/10.1029/jb084ib05p02243

723 Markušić, S., Stanko, D., Penava, D., Ivančić, I., Bjelotomić Oršulić, O., Korbar, T., & Sarhosis, V. (2021).
724 Destructive M6.2 Petrinja Earthquake (Croatia) in 2020—preliminary multidisciplinary research.
725 *Remote Sensing*, *13*(6), 1095. https://doi.org/10.3390/rs13061095

726 McGarr, A., & Fletcher, J. B. (2003). Maximum slip in earthquake fault zones, apparent stress, and
727 stick-slip friction. *Bulletin of the Seismological Society of America*, *93*(6), 2355–2362.
728 https://doi.org/10.1785/0120030037

729 Métois, M., D'Agostino, N., Avallone, A., Chamot-Rooke, N., Rabaute, A., Duni, L., Kuka, N., Koci, R., &
730 Georgiev, I. (2015). Insights on continental collisional processes from GPS data: Dynamics of the
731 peri-Adriatic belts. *Journal of Geophysical Research: Solid Earth*, *120*(12), 8701–8719.
732 https://doi.org/10.1002/2015jb012023

733 Metropolis, N., Rosenbluth, A. W., Rosenbluth, M. N., Teller, A. H., & Teller, E. (1953). Equation of state
734 calculations by fast computing machines. *The Journal of Chemical Physics*, *21*(6), 1087–1092.
735 https://doi.org/10.1063/1.1699114

736 Miranda, E. Brzev, S. Bijelic, N. Arbanas, Ž. Bartolac, M. Jagodnik, V. Lazarević, D. Mihalić Arbanas, S.

737 Zlatović, S. Acosta Vera, A. Archbold, J. Bantis, J. Blagojević, N. Borozan, J. Božulić, I. Cruz, C.
738 Dávalos, H. Fischer, E. Gunay, S. Hadzima-Nyarko, M. Heresi, P. Lignos, D. Lin, T. Marinković, M.
739 Messina, A. Miranda, S. Poulos, A. Scagliotti, G. Tomac, I. Tomić, I. Ziotopoulou, K. Žugić, Ž.
740 Robertson, I. (2021); JOINT RECONNAISSANCE REPORT (JRR)", in StEER- EERI: PETRINJA,
741 CROATIA DECEMBER 29, 2020, Mw 6.4 EARTHQUAKE. 2021.

742 Moreau, L., Hunter, A., Velichko, A., & Wilcox, P. (2014). 3-D reconstruction of sub-wavelength
743 scatterers from the measurement of scattered fields in elastic waveguides. *IEEE Transactions*
744 *on Ultrasonics, Ferroelectrics, and Frequency Control*, *61*(11), 1864–1879.
745 https://doi.org/10.1109/tuffc.2014.006619

746 Mueller, C. S. (1985). Source pulse enhancement by deconvolution of an empirical Green's function.
747 *Geophysical Research Letters*, *12*(1), 33–36. https://doi.org/10.1029/gl012i001p00033

748 Onwuemeka, J., Liu, Y., & Harrington, R. M. (2018). Earthquake stress drop in the Charlevoix Seismic
749 Zone, Eastern Canada. *Geophysical Research Letters*, *45*(22).
750 https://doi.org/10.1029/2018gl079382

751 Perrin, C., Waldhauser, F., & Scholz, C. H. (2021). The shear deformation zone and the smoothing of
752 faults with displacement. *Journal of Geophysical Research: Solid Earth*, *126*(5).
753 https://doi.org/10.1029/2020jb020447

754 Podvin, P., & Lecomte, I. (1991). Finite difference computation of traveltimes in very contrasted
755 velocity models: A massively parallel approach and its associated tools. *Geophysical Journal*
756 *International*, *105*(1), 271–284. https://doi.org/10.1111/j.1365-246x.1991.tb03461.x

757 Pousse-Beltran, L., Nissen, E., Bergman, E. A., Cambaz, M. D., Gaudreau, É., Karasözen, E., & Tan, F.
758 (2020). The 2020 mw 6.8 Elazığ (Turkey) earthquake reveals rupture behavior of the East
759 Anatolian fault. *Geophysical Research Letters*, *47*(13). https://doi.org/10.1029/2020gl088136

760 Radiguet, M., Cotton, F., Manighetti, I., Campillo, M., & Douglas, J. (2009). Dependency of near-field
761 ground motions on the structural maturity of the ruptured faults. *Bulletin of the Seismological*
762 *Society of America*, *99*(4), 2572–2581. https://doi.org/10.1785/0120080340

763 Rice, J. R. (2006). Heating and weakening of faults during earthquake slip. *Journal of Geophysical*
764 *Research: Solid Earth*, *111*(B5). https://doi.org/10.1029/2005jb004006

765 Rice, J. R., Sammis, C. G., & Parsons, R. (2005). Off-Fault secondary failure induced by a dynamic slip
766 pulse. *Bulletin of the Seismological Society of America*, *95*(1), 109–134.
767 https://doi.org/10.1785/0120030166

768 Ross, Z. E., Kanamori, H., Hauksson, E., & Aso, N. (2018). Dissipative intraplate faulting during the 2016
769 Mw 6.2 Tottori, Japan Earthquake. *Journal of Geophysical Research: Solid Earth*, *123*(2), 1631–
770 1642. https://doi.org/10.1002/2017jb015077

771 Roten, D., Olsen, K. B., & Day, S. M. (2017). Off-fault deformations and shallow slip deficit from
772 dynamic rupture simulations with fault zone plasticity. *Geophysical Research Letters*, *44*(15),
773 7733–7742. https://doi.org/10.1002/2017gl074323

774 Tan, Y., & Helmberger, D. (2010). Rupture directivity characteristics of the 2003 big bear sequence.
775 *Bulletin of the Seismological Society of America*, *100*(3), 1089–1106.
776 https://doi.org/10.1785/0120090074

777 Thingbaijam, K. K. S., Martin Mai, P., & Goda, K. (2017). New empirical earthquake source-scaling laws.
778 *Bulletin of the Seismological Society of America*, *107*(5), 2225–2246.

https://doi.org/10.1785/0120170017

Ustaszewski, K., Kounov, A., Schmid, S. M., Schaltegger, U., Krenn, E., Frank, W., & Fügenschuh, B. (2010). Evolution of the Adria-Europe plate boundary in the northern Dinarides: From continent-continent collision to back-arc extension. *Tectonics*, *29*(6), n/a-n/a. https://doi.org/10.1029/2010tc002668

Ustaszewski, K., Schmid, S. M., Fügenschuh, B., Tischler, M., Kissling, E., & Spakman, W. (2008). A map-view restoration of the Alpine-Carpathian-Dinaridic system for the Early Miocene. *Swiss Journal of Geosciences*, *101*(S1), 273–294. https://doi.org/10.1007/s00015-008-1288-7

Vallee, M. (2004). Stabilizing the empirical green function analysis: Development of the projected landweber method. *Bulletin of the Seismological Society of America*, *94*(2), 394–409. https://doi.org/10.1785/0120030017

Velasco, A. A.; Ammon, C. J., & Lay, T. (2004). Rupture directivity of the 3 november 2002 Denali Fault earthquake determined from surface waves. *Bulletin of the Seismological Society of America*, *94*(6B), S293–S299. https://doi.org/10.1785/0120040624

Venkataraman, A., & Kanamori, H. (2004). Observational constraints on the fracture energy of subduction zone earthquakes. *Journal of Geophysical Research: Solid Earth*, *109*(B5). https://doi.org/10.1029/2003jb002549

Viegas, G., Abercrombie, R. E., & Kim, W. (2010). The 2002 M5 Au Sable Forks, NY, earthquake sequence: Source scaling relationships and energy budget. *Journal of Geophysical Research: Solid Earth*, *115*(B7). https://doi.org/10.1029/2009jb006799

Wells, D. L., & Coppersmith, K. J. (1994). New empirical relationships among magnitude, rupture length, rupture width, rupture area, and surface displacement. *Bulletin of the Seismological Society of America*, *84*(4), 974–1002. https://doi.org/10.1785/bssa0840040974

Xiong, W., Yu, P., Chen, W., Liu, G., Zhao, B., Nie, Z., & Qiao, X. (2021). The 2020Mw 6.4 Petrinja earthquake: A dextral event with large coseismic slip highlights a complex fault system in northwestern Croatia. *Geophysical Journal International*, *228*(3), 1935–1945. https://doi.org/10.1093/gji/ggab440

Xu, S., Fukuyama, E., Yamashita, F., Kawakata, H., Mizoguchi, K., & Takizawa, S. (2023). Fault strength and rupture process controlled by fault surface topography. *Nature Geoscience*, *16*(1), 94–100. https://doi.org/10.1038/s41561-022-01093-z

Zielke, O., Galis, M., & Mai, P. M. (2017). Fault roughness and strength heterogeneity control earthquake size and stress drop. *Geophysical Research Letters*, *44*(2), 777–783. https://doi.org/10.1002/2016gl071700

Appendix

Supplementary material S1

Here we explain how to compute corner frequency as a function of source-receiver azimuth for a horizontal line source model, for unilateral and bilateral ruptures, as shown on Fig. 2c. Assuming a rise time equal to zero and a subshear rupture, the apparent source duration is equal to the difference between the last wave arrival time (emitted from one of the fault edge) and the first arrival time (emitted from the hypocenter). Assuming that the corner frequency is the inverse of the apparent rupture time, it can be obtained using Equations (S1.1) and (S2.2) for unilateral and bilateral ruptures, respectively:

$$f_{c_{app}} = \frac{f_c}{1-\alpha\, sin(i)\, cos(\theta)} \quad \text{(S1.1)}$$

$$f_{c_{app}} = \frac{1}{\mathrm{Max}\left(\frac{1}{fc}[1+\alpha\, sin(i)\, cos(\theta)]\right)} \quad \text{(S1.2)}$$

where α is the ratio between the rupture and the phase velocity, i is the takeoff angle of the considered phase, Θ is the source receiver azimuth and f_c is the average corner frequency.

Supplementary Figure S2: choice of the Empirical Green's Function

We tested several earthquakes to identify the most suitable candidate for the EGF method. Theoretically, the choice of earthquake for the EGF candidate should not impact the source time function. Although our findings demonstrate that our results are not significantly influenced by the choice of EGF, we observe notable uncertainties for certain stations. Figure S2.1 provides a comparison of various EGFs, illustrating examples of both good and poor station matches. The figure illustrates the variability observed for two different stations.

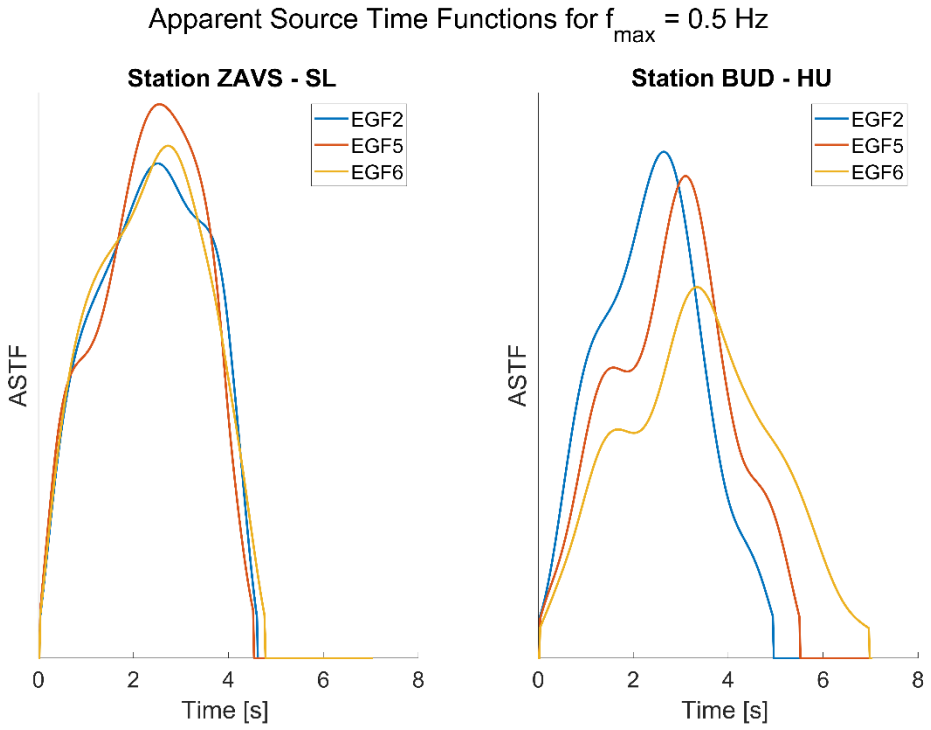

Figure S2.1. The examples of the good (on left) and the bad (on right) fit of apparent source time functions obtained by using different earthquakes as EGF (EGF2 – M4.7 event on Jan 6, 2021, at 17:01 UTC; EGF5 – M4.6 event on Dec 28, 2020, at 6:49 UTC; EGF6 – M5.1 event on Dec 28, 2020, at 5:28 UTC). EGF2 shows the most consistent results and therefore it was chosen as the representative earthquake for EGF.

Supplementary Figure S3

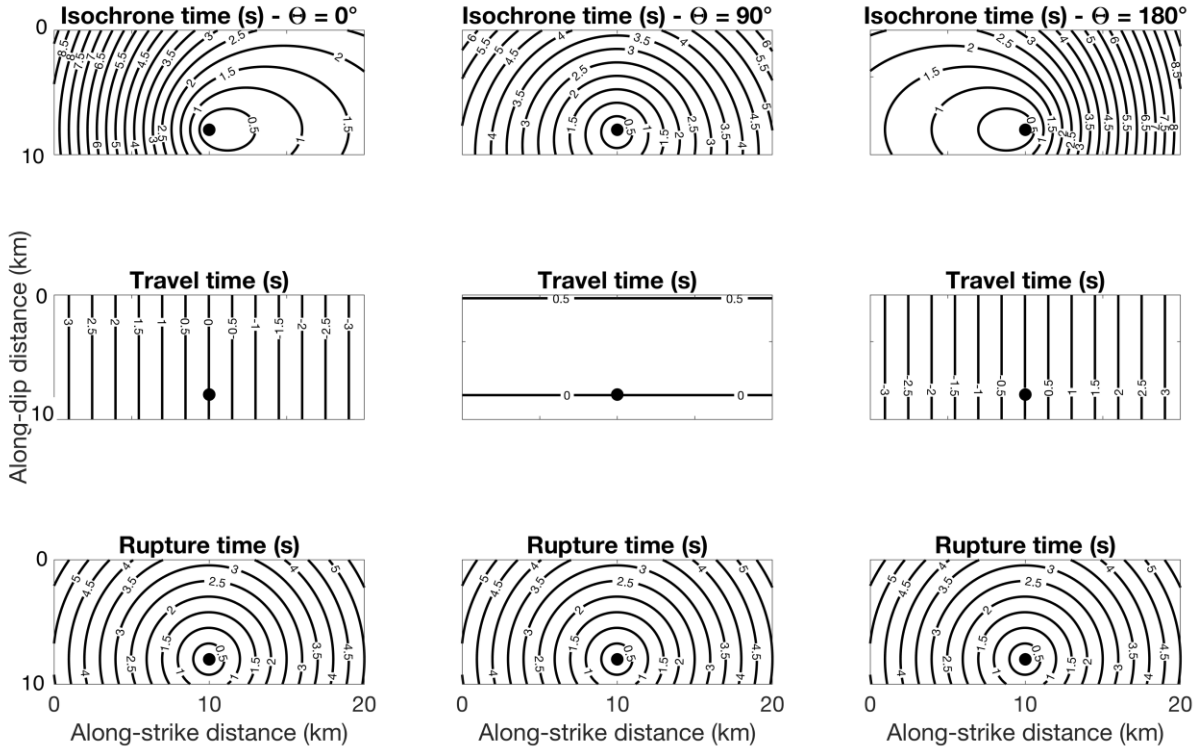

Figure S3.1: representation of rupture time, travel time and isochrones times for stations located at source-receiver azimuth of 0°, 90° and 180°. The isochrones time is the sum of rupture time and travel time. The rupture time is computed assuming a rupture propagating at a constant speed of 2 km/s from the hypocenter at 7.8 km/s. The rupture time is computed for horizontally propagating waves (Love waves) with phase velocity of 3.5 km/s.

Supplementary material S4: Love wave phase velocity tests

To choose a proper Love wave phase velocity value for our research, we computed theoretical dispersion curves for fundamental mode for Balkan velocity model (B.C.I.S., 1972). Due to the Balkan velocity model simplicity, we perform a few basic dispersion curve sensitivity tests by adding various softer shallow surface layers (Figure S4). Since we use Love waves filtered up to 0.5 Hz in our research, from figure S4.1 we can see that it is hard to choose one exact *c* value for our research. In contrary, we tested our model and its sensitivity to the whole range of *c* values between 3000 m/s and 4000 m/s. The best model is computed using *c* = 3500 m/s.

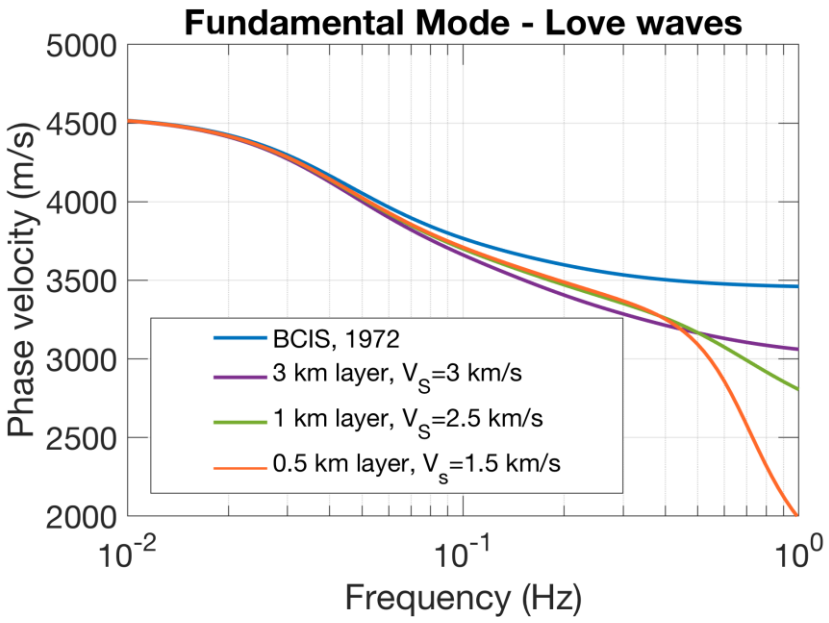

Figure S4.1. Theoretical dispersion curves of Love waves computed in fundamental mode for the Balkan velocity model (B.C.I.S., 1972).

Supplementary material S5: comparison of the obtained finite source parameters for various initial parameters

To assess the sensitivity of our model concerning the initially defined input parameters, we conducted several tests described hereafter, and the results of which are compiled in Table S5.1:

1. we conducted an inversion with a nucleation depth fixed at 8 km, following Baize et al. (2022). Even with a fixed depth, the results align with our best model, suggesting a slow rupture velocity and consistent rupture dimensions. Note, however, that the patch of significant slip does not reach the surface.

2. while using ASTFs computed with f_{max} = 0.5 Hz for balancing fit quality with model detail, we performed an inversion using f_{max} = 0.1 Hz. This lower frequency dataset leads to a slightly simpler slip model and a higher fit. The rupture velocity slightly increases (~0.6V_S), but still remains lower than commonly reported values (Heaton, 1990).

3. examining the impact of convolving the ASTFs with Boxcar functions, we performed kinematic inversion with raw ASTFs, using f_{max} = 0.5 Hz. Results align with the preferred model but yield the lowest fit between simulated and observed ASTFs.

4. introducing variability to rupture velocity using control points over the fault plane, we found that the fit does not increase significantly, indicating that our data lacks the resolution to describe spatial variability of rupture velocity. Note that including V_R perturbations does not alter the main conclusions. Further, we checked that using 3 or 5 control points does not significantly change the level of fit. We considered 4 control points as a good compromise to map slip complexity keeping a reasonable number of parameters.

5. uneven azimuthal coverage in the data, biased toward the northwest, was addressed by assigning weights based on source-to-station azimuthal class. We checked that inversion with weighted or unweighted data yields similar results to the best model, indicating that irregular azimuthal coverage seems to plays a minor role.

6. we tested the impact on uncertainty of the phase velocity of Love waves (c). The results remain consistent across different c values (3 km/s to 4 km/s).

Table S5 reports the obtained source parameters for each inversion/ The best model is the one obtained using ASTFs convolved with a boxcar function, obtained with f_{max}=0.5 Hz, using the same

weight for each station with same weights, with free nucleation point position and four slip control points.

Table S5. Finite source parameters and level of fit between observed and simulated ASTFs for inversions with various initial parameters. Our "best" reference model is shown for comparison. V_R is rupture velocity, τ is rise time, L_{eff} is effective rupture length, W_{eff} is effective rupture width, and D_{max} is maximum value of the slip. V_s = 3400 m/s is a shear wave velocity from Balkan model (B.C.I.S., 1972) and c is a Love wave phase velocity. f_{max} is the maximum frequency used in the ASTF deconvolution. R^2 is the coefficient of determination, calculated as the squared correlation between the observed and simulated data. The closer the R^2 value is to 1, the simulated model better explains the observed data.

Tested scenarios	**BEST MODEL**	Raw ASTFs*	f_{max} = 0.1 Hz	Weighted data **	Nucleation fixed at d = 8 km	c [m/s]		Slip control points
						3000	4000	5
V_R	1420 m/s ≈0.4V_s	1550 m/s ≈0.5V_s	1930 m/s ≈0.6V_s	1330 m/s ≈0.4V_s	1660 m/s ≈0.5V_s	1500 m/s ≈0.4V_s	1640 m/s ≈0.5V_s	1340 m/s ≈0.4V_s
τ	1.3	1	2.1	0.9	0.9	1.7	1.9	1.2
L_{eff}	6.5	6.5	6.5	7.0	7.5	7	5.5	6.5
W_{eff}	6.0	6.5	6.0	5.5	6.0	6.0	6.5	6.0
D_{max}	5.7	4.8	6.0	6.0	4.6	6.0	6.0	6.0
R^2	0.92	0.84	0.96	0.90	0.91	0.92	0.92	0.92

* ASTFs cleared from bumps but not convolved with a Box-Car function

** Different weights are assigned to ASTFs with respect to the number of stations in given azimuthal ranges like described in section 3.2.

Supplementary Figure S6: Evolution of cost with iterations in the first stage of kinematic inversion

Figure S6 shows the evolution of the cost function value with iterations of the preformed first stage of the kinematic inversion by showing Root Mean Square (RMS) of accepted candidates. A descending trend of the cost value, obtained by employing a simulated annealing (SA) cooling scheme, is evident. A dashed blue line represents all tested models and a magenta line represents accepted models.

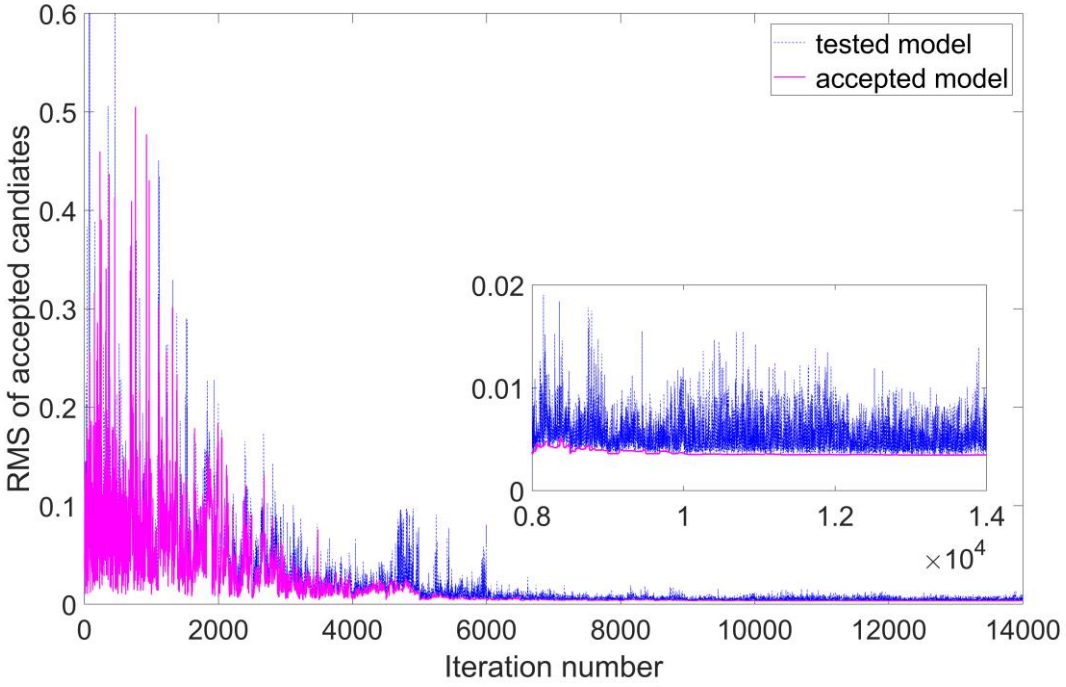

Figure S6. Evolution of the cost function value with iterations. The dashed blue line represents the tested models and the magenta line, the accepted models. The inserted box shows the zoom of last iterations.